

Thermal Conductivity of the Martian Soil at the InSight Landing site from HP³ Active Heating Experiments

Matthias Grott¹, T. Spohn², Joerg Knollenberg¹, Christian Krause³, Troy L. Hudson⁴, Sylvain Piqueux⁴, N. Müller⁵, Matthew P. Golombek⁶, Christos Vrettos⁷, Eloise Marteau⁴, Seiichi Nagihara⁸, Paul Morgan⁹, J.P. Murphy¹⁰, Matthew Adam Siegler¹¹, Scott D. King¹², Suzanne E Smrekar⁴, and William Bruce Banerdt¹³

¹DLR Institute for Planetary Research

²International Space Science Institute (ISSI)

³DLR Institute of Space Systems

⁴Jet Propulsion Laboratory

⁵German Aerospace Center (DLR), Institute of Planetary Research

⁶California Institute of Technology/JPL

⁷Technical University of Kaiserslautern

⁸Texas Tech University

⁹Colorado School of Mines

¹⁰Virginia Polytechnic Institute and State University

¹¹Planetary Sciences Institute

¹²Virginia Tech

¹³Jet Propulsion Lab (NASA)

November 26, 2022

Abstract

The heat flow and physical properties package (HP³) of the InSight Mars mission is an instrument package designed to determine the martian planetary heat flow. To this end, the package was designed to emplace sensors into the martian subsurface and measure the thermal conductivity as well as the geothermal gradient in the 0-5 m depth range. After emplacing the probe to a tip depth of 0.37 m, a first reliable measurement of the average soil thermal conductivity in the 0.03 to 0.37 m depth range was performed. Using the HP³ mole as a modified line heat source, we determined a soil thermal conductivity of $0.039 \pm 0.002 \text{ W m}^{-1} \text{ K}^{-1}$, consistent with the results of orbital and in-situ thermal inertia measurements. This low thermal conductivity implies that 85 to 95% of all particles are smaller than $104\text{-}173 \mu\text{m}$ and suggests that any cement contributing to soil cohesion cannot significantly increase grain-to-grain contact areas by forming cementing necks, but could be distributed in the form of grain coatings instead. Soil densities compatible with the measurements are $1211\text{-}113^{+149} \text{ kg m}^{-3}$, indicating soil porosities of 61 %.

Thermal Conductivity of the Martian Soil at the InSight Landing site from HP³ Active Heating Experiments

M. Grott¹, T. Spohn^{1,2}, J. Knollenberg¹, C. Krause³, T.L. Hudson⁴, S.
Piqueux⁴, N. Mller¹, M. Golombek⁴, C. Vrettos⁵, E. Marteau⁴, S. Nagihara⁶,
P. Morgan⁷, J.P. Murphy⁸, M. Siegler^{9,10}, S.D. King⁸, S.E. Smrekar⁴, W.B.
Banerdt⁴

¹German Aerospace Center (DLR), Institute of Planetary Research, Berlin, Germany

²International Space Science Institute (ISSI), Bern, Switzerland

³German Aerospace Center (DLR), MUSC Space Operations and Astronaut Training, Cologne, Germany

⁴Jet Propulsion Laboratory, California Institute of Technology, Pasadena, USA

⁵Department of Civil Engineering, Technical University Kaiserslautern, Germany

⁶Department of Geosciences, Texas Tech University, Lubbock, USA

⁷Colorado Geological Survey, Colorado School of Mines, Golden, USA

⁸Virginia Polytechnic Institute and State University, Blacksburg, USA

⁹Planetary Science Institute, Tucson, AZ, USA

¹⁰Southern Methodist University, Dallas, TX, USA

Key Points:

- The Heat Flow and Physical Properties Package (HP³) measured the average thermal conductivity of the martian soil.
- Average soil thermal conductivity in the 0.03 to 0.37 m depth range is $0.039 \pm 0.002 \text{ W m}^{-1} \text{ K}^{-1}$.
- This implies that 85 to 95% of all particles are smaller than 104-173 μm .

24 **Abstract**

25 The heat flow and physical properties package (HP³) of the InSight Mars mission is an
 26 instrument package designed to determine the martian planetary heat flow. To this end,
 27 the package was designed to emplace sensors into the martian subsurface and measure
 28 the thermal conductivity as well as the geothermal gradient in the 0-5 m depth range.
 29 After emplacing the probe to a tip depth of 0.37 m, a first reliable measurement of the
 30 average soil thermal conductivity in the 0.03 to 0.37 m depth range was performed. Us-
 31 ing the HP³ mole as a modified line heat source, we determined a soil thermal conduc-
 32 tivity of $0.039 \pm 0.002 \text{ W m}^{-1} \text{ K}^{-1}$, consistent with the results of orbital and in-situ ther-
 33 mal inertia measurements. This low thermal conductivity implies that 85 to 95% of all
 34 particles are smaller than 104-173 μm and suggests that any cement contributing to soil
 35 cohesion cannot significantly increase grain-to-grain contact areas by forming cement-
 36 ing necks, but could be distributed in the form of grain coatings instead. Soil densities
 37 compatible with the measurements are $1211_{-113}^{+149} \text{ kg m}^{-3}$, indicating soil porosities of 61
 38 %.

39 **Plain Language Summary**

40 The heat flow and physical properties package (HP³) of the InSight Mars mission
 41 is an instrument package designed to measure the martian planetary heat flow by de-
 42 termining temperature and thermal conductivity in the 0 to 5 m depth range. After in-
 43 serting the probe to a tip depth of 0.37 m, a first thermal conductivity measurement was
 44 performed, and average soil conductivity in the 0.03 to and 0.37 m depth range was found
 45 to be $0.039 \pm 0.002 \text{ W m}^{-1} \text{ K}^{-1}$. Upper limits on soil grain size can be derived from ther-
 46 mal conductivity by a comparison with laboratory measurements under martian atmo-
 47 spheric conditions, and the determined conductivity values indicate that the majority
 48 of particles must be smaller than 104-173 μm . The low conductivity further suggests that
 49 soil cementation cannot significantly contribute to soil thermal conductivity by forming
 50 cementing necks. Rather, any cement is likely distributed in the form of grain coatings,
 51 which have little influence on thermal properties. The soil densities compatible with our
 52 thermal measurements are $1211_{-113}^{+149} \text{ kg m}^{-3}$, indicating significant soil porosities of about
 53 60%.

1 Introduction

The martian near surface layer consists of sand-sized as well as dust-sized particles (Christensen & Moore, 1992) interspersed with larger rocks, and its detailed structure depends on the deposition process as well as subsequent surface modifications by aeolian and fluvial activity. Under present martian atmospheric conditions sand-sized particles in the 100-600 μm size range can be mobilized by winds (Kok et al., 2012), and dust particles of typical sizes around 2.5 μm are suspended in the atmosphere and can reach the ground in the form of airfall (Pollack et al., 1979), such that aeolian processes are generally recognized to be the prevalent surface modification process on Mars today.

The thermal conductivity is a fundamental physical property of the surface material and determines the rate at which heat can be transferred from the interior to the surface and vice versa. Heat is transported through grain-to-grain contacts, conduction through the pore-filling gas, as well as radiation between individual grains, and the conductivity of the martian soil holds information on the soils bulk porosity, composition, grain size (Presley & Christensen, 1997; Presley & Craddock, 2006; Piqueux & Christensen, 2009a), as well as the state of cementation or induration (Presley et al., 2009; Piqueux & Christensen, 2009b). Thermal properties of the martian soil can thus provide critical information to better understand the local, regional and global geologic processes modifying the surface of Mars, including material redeposition as well as soil-atmosphere interactions. The latter can result in cementation or induration by salts, which may be common on Mars (Mutch et al., 1977; Ditteon, 1982; Moore et al., 1999; Banin et al., 1992; Haskin et al., 2005; Hurowitz et al., 2006) and can have a significant influence on thermal properties by increasing the contact area between individual grains (Piqueux & Christensen, 2009a).

Thermal properties of the martian soil have primarily been estimated from remote sensing infrared observations conducted from orbit (Kieffer et al., 1977; Palluconi & Kieffer, 1981; Mellon et al., 2000; Putzig & Mellon, 2007; Golombek et al., 2008), but some investigations have also been performed on the ground (Ferguson et al., 2006; Hamilton et al., 2014; Golombek, Warner, et al., 2020). In general, thermal inertia

$$\Gamma = \sqrt{k\rho c_p} \quad (1)$$

is derived from measurements of the surface brightness temperature, where k is thermal conductivity, ρ is density, and c_p is specific heat capacity. Globally, thermal inertia was

85 found to have a bimodal distribution (Kieffer et al., 1977; Mellon et al., 2000; Putzig &
86 Mellon, 2007), with peaks around 75 and 250 J m⁻² K⁻¹ s^{-1/2}, representing dust cov-
87 ered and dust free surfaces, respectively. Higher thermal inertia units are associated with
88 impact craters and the associated ejecta (Mellon et al., 2000), but it has also been ar-
89 gued that high thermal inertia may be related to soil induration often referred to as duri-
90 crust (Jakosky & Christensen, 1986).

91 Thermal conductivity can be interpreted in terms of soil grain size (e.g., Hamilton
92 et al. (2014)) by a comparison with results from laboratory experiments (Presley & Chris-
93 tensen, 1997; Presley & Craddock, 2006). Estimates of grain size were found to be ro-
94 bust if cementation of the soil is minimal and indurated surface layers are much thin-
95 ner than the diurnal skin depth. Edwards et al. (2018) compared orbital and rover re-
96 sults with grain size estimates derived from direct microscopic imaging at a dune field
97 in Gale Crater and found that particle sizes derived from the different datasets yield con-
98 sistent results, indicating that grain sizes of homogeneous material derived from tem-
99 perature measurements are reliable.

100 Out of the few measurements from the ground, most have been performed using
101 radiometric methods, and thermal inertia at the Mars Exploration Rover landing sites
102 was determined using the mini-TES instrument for a number of bedforms. Particle sizes
103 derived from these measurements were 45 to 415 μm and were generally found to be con-
104 sistent with those derived from Microscopic Imager data. Although some discrepancies
105 in the data analysis remained, results indicated that in most cases the relationship be-
106 tween thermal inertia and effective particle size as determined in the laboratory (Pres-
107 ley & Christensen, 1997) also holds for the mini-TES observations (Ferguson et al., 2006).

108 At Gale Crater (4.59°N, 137.44°E) thermal inertia determined using the REMS GTS
109 sensor (Gómez-Elvira et al., 2012) ranged from 265375 J m⁻² K⁻¹ s^{-1/2} along the Cu-
110 riosity rover’s traverse (Hamilton et al., 2014). Furthermore, thermal inertia was found
111 to be 180-215 J m⁻² K⁻¹ at a sand patch called Rocknest. Using thermal inertia as a
112 proxy for grain size and comparing results with those from laboratory experiments (Pres-
113 ley & Christensen, 1997), thermal inertia was found to be generally consistent with par-
114 ticle sizes determined from images (Edgett et al., 2013; Yingst et al., 2013). Millimeter
115 sized particles dominate along the rover’s traverse, and thermal inertia at Rocknest in-
116 dicates particle sizes around 200 μm .

117 To date, the only direct thermal measurement using needle probes was performed
 118 by the thermal and electrical permittivity probe (TECP) during the Phoenix mission,
 119 which landed in Vastitas Borealis at 68.22°N 234.25°E and investigated the martian po-
 120 lar regions in a search for subsurface ice (Mellon et al., 2009). TECP measurements in-
 121 dicated a thermal conductivity of $0.085 \text{ W m}^{-1} \text{ K}^{-1}$ and an average ρc_p equal to $1.05 \cdot$
 122 $10^6 \text{ J m}^{-3} \text{ K}^{-1}$ (Zent et al., 2010). The dry material above the ground ice was there-
 123 fore found to be a good thermal insulator, protecting the ice from large temperature ex-
 124 cursions during noontime.

125 Here we report on direct thermal conductivity measurements at the InSight land-
 126 ing site in Homestead hollow, located in the Elysium Planitia region (4.50°N, 135.62°E)
 127 (Banerdt et al., 2020). In the region, the regolith is estimated to constitute a 3-17 m thick
 128 layer of broken up material (Warner et al., 2017), and regolith thickness at the landing
 129 site itself is estimated to be close to 3 m (Golombek, Kass, et al., 2020). The stratigra-
 130 phy exposed underneath the InSight lander indicates layering consistent with a surficial
 131 dust layer over thin unconsolidated sand, underlain by a cohesive duricrust, which ap-
 132 pears to be at least 5-10 cm thick (Golombek, Warner, et al., 2020) and may be under-
 133 lain by unconsolidated cohesive sand mixed with rocks beneath (Hudson et al., 2020).

134 Thermal inertia at the landing site was found to be 160 to $230 \text{ J m}^{-2} \text{ K}^{-1} \text{ s}^{-1/2}$
 135 (Golombek, Warner, et al., 2020), consistent with estimates obtained by the Thermal
 136 Emission Spectrometer (TES) (Mellon et al., 2000; Putzig & Mellon, 2007), which de-
 137 termined inertias of $\sim 200 \text{ J m}^{-2} \text{ K}^{-1} \text{ s}^{-1/2}$ from orbit. Further, the Thermal Emission
 138 Imaging System (THEMIS) of the Mars Odyssey mission shows a high homogeneity of
 139 thermal properties at the 100 m scale and a median thermal inertia of around 180 J m^{-2}
 140 $\text{K}^{-1} \text{ s}^{-1/2}$ near the landing site (Golombek et al., 2017; Golombek, Kass, et al., 2020),
 141 indicating that measurements performed by the InSight radiometer are representative
 142 of the regional soil properties. In addition, the lack of significant seasonal variations in
 143 thermal inertia suggest the same material extends down to a few tens of centimeters depth.

144 2 Probe Emplacement

145 The InSight Mars mission (Banerdt et al., 2020) landed in the Elysium Planitia re-
 146 gion on Mars (Golombek et al., 2018; Golombek, Williams, et al., 2020; Golombek, Warner,
 147 et al., 2020) on November 26, 2018, and installed a geophysical and meteorological sta-

148 tion at the landing site. One of InSight’s payloads is the Heat Flow and Physical Prop-
149 erties Package (HP³), which was designed to make the first direct measurement of the
150 martian planetary heat flow (Grott et al., 2007; Spohn et al., 2018; Grott et al., 2019).
151 To determine heat flow, HP³ is designed to emplace 14 temperature sensors to a target
152 depth of 5 m using a self-hammering penetrator called ”the mole”. During descent, the
153 depth of the sensors is determined from the attitude of the mole with respect to verti-
154 cal using static tiltmeters, while simultaneously measuring the amount of paid-out tether.
155 Furthermore, a profile of subsurface thermal conductivity was planned to be determined
156 at 50 cm depth intervals using the mole as a modified line heat source (Hammerschmidt
157 & Sabuga, 2000).

158 After an initial phase of surface characterization, first the InSight seismometer and
159 then the HP³ were deployed onto the surface by the lander’s robotic arm (Golombek,
160 Williams, et al., 2020). HP³ then started hammering on Sol 92 of the mission (Febru-
161 ary 28, 2019), but the depth sensor did not show significant progress despite the fact that
162 3600 hammering strokes had been executed. Hammering was recommended at the next
163 opportunity, and an additional 5000 strokes were executed on Sol 94 (March 2, 2019).
164 At this point it became clear that the probe did not penetrate as expected. In an attempt
165 to resolve the anomaly the HP³ support structure was removed from above the mole, ex-
166 posing the probe for further investigation on Sol 209 (June 29, 2019).

167 Insufficient friction to compensate for recoil during hammering was identified as
168 the basic cause of the penetration anomaly (Hudson et al., 2020). Using the lander’s robotic
169 arm, friction was provided by first pressing on the side of the mole (Sol 302 to Sol 407;
170 October 2, 2019, to January 18, 2020) and later recoil was compensated by pressing di-
171 rectly onto the back of the mole (Sol 427 to Sol 557; February 8, 2020, to June 20, 2020).
172 In this way, it was possible to bury the back of the mole step-wise to approximately 3
173 cm below the surface using an additional 1700 strokes in total. The average penetration
174 rate during this time was 0.15 mm per stroke. Together with a mole length of 40 cm and
175 a mole inclination of 30° with respect to vertical, this depth corresponds to a mole tip
176 depth of approximately 37 cm. Therefore, the measurements presented here represent
177 average thermal conductivity in the 0.03 to 0.37 m depth range.

178 The left hand panel of Fig. 1 shows the configuration of the mole after reaching
179 the maximum depth possible using direct support from the robotic arm to compensate



Figure 1. Left: Mole configuration on Sol 598 before scraping soil into the mole pit. Right: Sol 674 after filling the pit and after retracting the robotic arm. The active heating experiment reported here was conducted in this configuration.

180 recoil. Tilt of the mole as well as a highly cohesive soil layer and a sizeable pit surround-
 181 ing the mole are apparent. After filling some material into the pit the robotic arm pressed
 182 on the mole, but the following hammering attempts between Sol 618 and Sol 645 (Au-
 183 gust 22 to September 19, 2020) showed no clear indication of significant (>1 cm) fur-
 184 ther depth progress. Subsequent activities focused on filling the pit to increase friction
 185 between the mole and soil, but no additional hammering was performed before the TEM-
 186 A measurement on Sol 680.

187 During the period of mole recovery activities, a number of active heating exper-
 188 iments to determine the thermal conductivity of the soil were performed (Sols 97, 116,
 189 211, 380, and 536). However, all of these suffered from the fact that the mole was not
 190 fully buried, thus providing reduced thermal contact to the soil. In addition, direct so-
 191 lar illumination induced a large background temperature variation superimposing the
 192 heating curve with a strong diurnal signal and complicating data analysis. In contrast,
 193 the mole was fully buried during the measurement conducted on Sol 680, and the cor-
 194 responding configuration is shown in the right hand panel of Fig. 1. During the mea-
 195 surement, the mole was protected from direct insolation and the residual diurnal tem-
 196 perature amplitude was only 4 K at the effective depth of the temperature sensors in the
 197 mole. In the following we report on the results of the Sol 680 measurement and the av-
 198 erage soil thermal conductivity in the 0.03 to 0.37 cm depth range.

199 **3 Modeling**

200 **3.1 Data Reduction**

201 HP³ measures thermal conductivity by operating the mole as a modified line heat
 202 source (Jaeger, 1956; Hammerschmidt & Sabuga, 2000). During a measurement, a de-
 203 fined amount of heat is provided to the mole’s outer hull and the resulting temperature
 204 rise is monitored as a function of time (Spohn et al., 2018; Grott et al., 2019). Soil ther-
 205 mal conductivity can then be determined from the rate of self heating, where a fast tem-
 206 perature increase corresponds to low thermal conductivity and vice versa. Note that this
 207 method is slightly different from the dual needle technique applied by the TECP probe
 208 (Zent et al., 2010), which generates a heat pulse at one needle and measures the tem-
 209 perature rise at a second needle.

210 Before the active heating experiment was started on Sol 681, the background tem-
 211 perature drift was monitored for 2 Sols. Operations were then timed such that heating
 212 started at 21:00 local true solar time (LTST), thus allowing temperature perturbations
 213 induced by direct insolation to decay, while at the same time maximizing the time be-
 214 fore sunrise. Furthermore, care was taken to ensure that sources of shadow like the robotic
 215 arm did not move during the experiment to minimize day-to-day temperature variations.
 216 The heating power of the probe was set to 2 W to increase the temperature rise during
 217 the heating phase to the greatest possible amount, thereby increasing the signal to noise
 218 ratio with respect to background temperature variations.

219 Temperature data obtained for the active heating experiment conducted between
 220 Sols 680 and 682 are shown in Fig. 2(a), where temperature is given as a function of LTST
 221 and color-code indicates the Sol of the measurement. The heating power dissipated in
 222 the probe is shown in panel (b) of the figure for the same time frame, demonstrating that
 223 heating power was kept constant by the control loops in the HP³ electronics during the
 224 experiment. As shown, temperature was monitored on Sol 680 and Sol 681 before switch-
 225 ing on the heaters at 21:00 LTST on Sol 681. The background temperatures show a di-
 226 urnal amplitude of 4 K, with maximum temperatures reached at 16:40 and minimum tem-
 227 peratures at 8:00 LTST. As is evident from the figure, background temperatures are highly
 228 repeatable, and we found day-to-day variations to be smaller than 80 mK.

229 We then extracted the heating curve between Sol 681 21:00 LTST and Sol 682 21:00
 230 LTST by subtracting the background temperatures from Sol 680 21:00 LTST to Sol 681
 231 21:00 LTST from the data, and temperatures were then referenced to the start of the
 232 heating interval at 21:00 LTST on Sol 681 to obtain the temperature rise ΔT as a func-
 233 tion of time, which is shown in Fig. 2(c). Furthermore, data was downsampled from 5548
 234 to 1000 points by linear interpolation to save computing time. A slight change of slope
 235 caused by background temperature fluctuations is visible during the final hours of heat-
 236 ing, and we disregard data at times later than 21 h 40 min after start of heating for the
 237 data inversion below. Furthermore, data before 1 h was also not considered, as this part
 238 of the heating curve is most sensitive to the unknown contact conductance between probe
 239 and soil. Therefore, to reduce uncertainties associated with the unknown contact, we per-
 240 formed inversions between 1 h and 21 h 40 min only. Fig. 2(d) shows the logarithmic
 241 time derivative of the heating curve to illustrate the amount of scatter, which is caused
 242 by short-term temperature fluctuations resulting from the diurnal temperature forcing.

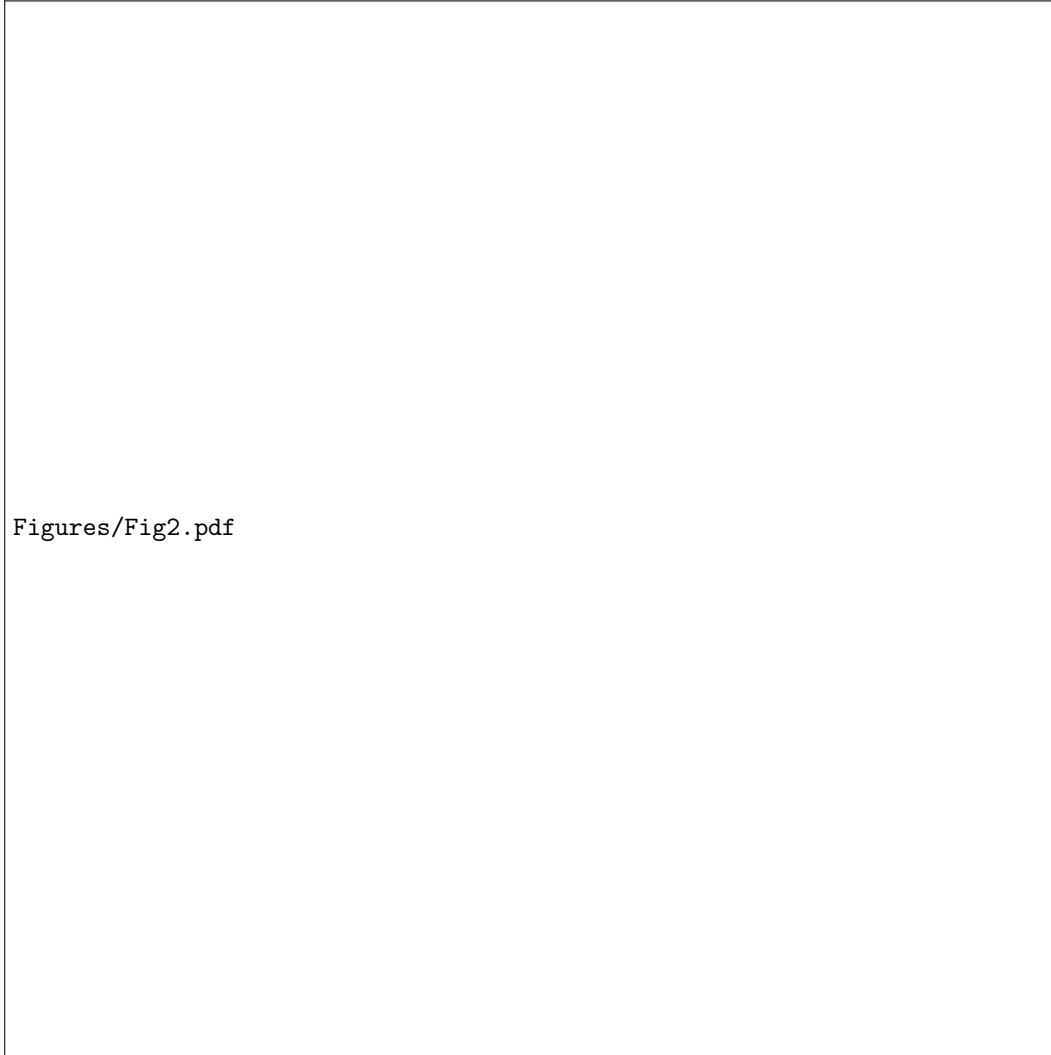


Figure 2. Illustration of steps taken during data reduction. (a) Temperature as a function of local true solar time (LTST) for the three Sols of the experiment. Heating was activated on Sol 681 at 21:00 LTST and continued for 24 h. (b) Heating power as a function of local time for the same time frame. (c) Heating curve (temperature rise as a function of time) extracted from the data shown in (a) (see text for details). (d) Logarithmic time derivative of the temperature rise shown in (c) as a function of time.

243 Therefore, rather than using the logarithmic time derivative as a fitting function (Spohn
 244 et al., 2018; Grott et al., 2019), we use the heating curve itself to determine soil ther-
 245 mal conductivity in the following.

246 3.2 Data Inversion

247 We used forward modeling of the heating curve to determine the admissible range
 248 of soil parameters. The temperature response to heating of the mole was modeled us-
 249 ing a finite element model in cylindrical geometry. The model encompasses a reduced
 250 thermal model of the mole including the hull, motor, hammering mechanism, heaters,
 251 the science tether connecting the mole to the electronics, and the surrounding soil. The
 252 model solves the initial value problem posed by the heat conduction equation and as-
 253 sociated boundary conditions starting from thermal equilibrium, and thermophysical prop-
 254 erties of the mole and soil need to be prescribed. In addition, thermal contact conduc-
 255 tance between the mole and soil is explicitly taken into account, as this can have a sig-
 256 nificant influence on the temperature rise during the first part of the experiment (also
 257 compare Grott et al. (2010) for the lunar case). Details of the finite element model are
 258 given in Grott et al. (2019).

259 To determine the range of admissible soil parameters, we ran Monte-Carlo simu-
 260 lations varying soil thermal conductivity k , soil density ρ , as well as thermal contact con-
 261 ductance between probe and soil H to determine parameter combinations which allowed
 262 us to fit the heating curve within admissible limits. The latter were defined based on the
 263 observation that background temperature drift was reproducible to within 80 mK on con-
 264 secutive sols. Furthermore, probe calibration may have drifted as a consequence of be-
 265 ing exposed to diurnal temperature cycles. Temperature drift can result in an additional
 266 0.4% uncertainty for temperature difference measurements (Grott et al., 2019), and given
 267 a temperature rise of 37.3 K during the measurement, potential sensor drift adds an ad-
 268 ditional uncertainty of 150 mK. Assuming Gaussian uncertainty propagation, total ad-
 269 missible uncertainty δT is then given by

$$\delta T = \sqrt{\delta T_{var}^2 + \delta T_{drift}^2} \quad (2)$$

270 where δT_{var} and δT_{drift} are the uncertainty contributions stemming from day to day vari-
 271 ations and potential sensor drift, respectively. Therefore, we require the forward model
 272 to reproduce temperatures to within $\delta T = 170$ mK.



Figure 3. Illustration of the temperature distribution in the finite element model at the end of the heating period. The soil thermal conductivity used in the model was $0.04 \text{ W m}^{-1} \text{ K}^{-1}$, heating power was 2 W , the back of the mole was assumed to be 3 cm below the surface.

273 For each model run of the Monte-Carlo simulation, the modeled temperature $T_{mod}(t, k, \rho, H)$
 274 was then compared to the measured temperature rise $T_{dat}(t)$ and the root mean square
 275 deviation between the two quantities was determined according to

$$\Delta T_{rms}(k, \rho, H) = \left(\sum_{i=1}^n (T_{mod}(t_i, k, \rho, H) - T_{dat}(t_i))^2 / n \right)^{\frac{1}{2}} \quad (3)$$

276 Here, $n = 1000$ is the number of measurement points, and $t_1 = 1 \text{ h}$ and $t_n = 21 \text{ h } 40$
 277 min correspond to the beginning and the end of the inversion interval, respectively (see
 278 above). In case $\Delta T_{rms}(k, \rho, H) < \delta T$, the combination of parameters k , ρ , and H was
 279 considered admissible

280 An illustration of the results of the finite element model is shown in Fig. 3, where
 281 the color coded temperature field is shown for the best fitting model. Heating was ac-
 282 tive for $21 \text{ h } 40 \text{ min}$ at a heating power of 2 W , and soil thermal conductivity was as-
 283 sumed to be $0.039 \text{ W m}^{-1} \text{ K}^{-1}$. Although heat transport is primarily in the radial di-
 284 rection, some heat is also lost along the mole axis, illustrating the need to consider a probe
 285 with finite length in contrast to analytical solutions for this type of heat conduction prob-

286 lem (Jaeger, 1956). The computational domain has a diameter of 0.4 m, large enough
 287 to minimize boundary effects, and the heat from the mole penetrates a few centimeters
 288 into the soil.

289 An additional constraint that can be considered to restrict the range of admissi-
 290 ble models is posed by the surface thermal inertia, which is sensitive to the upper ~ 0.07
 291 m of the soil and ranges from 160 to 230 $\text{J m}^{-2} \text{K}^{-1} \text{s}^{-1/2}$ at the landing site (Golombek,
 292 Warner, et al., 2020). If soil parameters are assumed to be constant as a function of depth,
 293 parameter combinations determined here should also satisfy this additional constraint.
 294 Here we assume a soil heat capacity c_p of 630 $\text{J kg}^{-1} \text{K}^{-1}$ (Morgan et al., 2018) to con-
 295 vert density and thermal conductivity into thermal inertia Γ , and models satisfying the
 296 additional constraint $160 \leq \Gamma \leq 230 \text{ J m}^{-2} \text{K}^{-1} \text{s}^{-1/2}$ (Golombek, Warner, et al., 2020;
 297 Piqueux et al., 2021) will be discussed in addition to the models fitting the heating curve
 298 only.

299 4 Results

300 4.1 Monte Carlo Simulations

301 We calculated forward models of the heating experiment varying the soil thermal
 302 conductivity k , density ρ , as well as the thermal contact conductance between probe and
 303 soil H , searching for models which fit measured temperatures within error bounds and
 304 within the constraints posed by the surface thermal inertia. To reduce the number of Monte-
 305 Carlo simulations, we first conducted a series of test calculations, varying thermal con-
 306 ductivity between $0.01 \leq k \leq 0.1 \text{ W m}^{-1} \text{K}^{-1}$, soil density between $600 \leq \rho \leq 1800$
 307 kg m^{-3} , and contact conductance between $3 \leq H \leq 250 \text{ W m}^{-2} \text{K}^{-1}$ to narrow down
 308 the parameter space. We found that only conductivities between 0.034 and 0.045 W m^{-1}
 309 K^{-1} yielded admissible models, such that the full Monte-Carlo run was restricted to these
 310 conductivities in the following. In total, 45000 models were calculated and parameters
 311 were assumed to be equally distributed in the above intervals. For each draw of param-
 312 eters, the resulting model was compared with the data and 229 models reproduced mea-
 313 sured temperatures within errorbounds. Out of these models, 102 satisfied the additional
 314 constraint posed by the surface thermal inertia.

315 Results of the calculations are shown in Fig. 4, where the best fit model is shown
 316 together with the data and associated uncertainties in panel (a). As is evident, the model

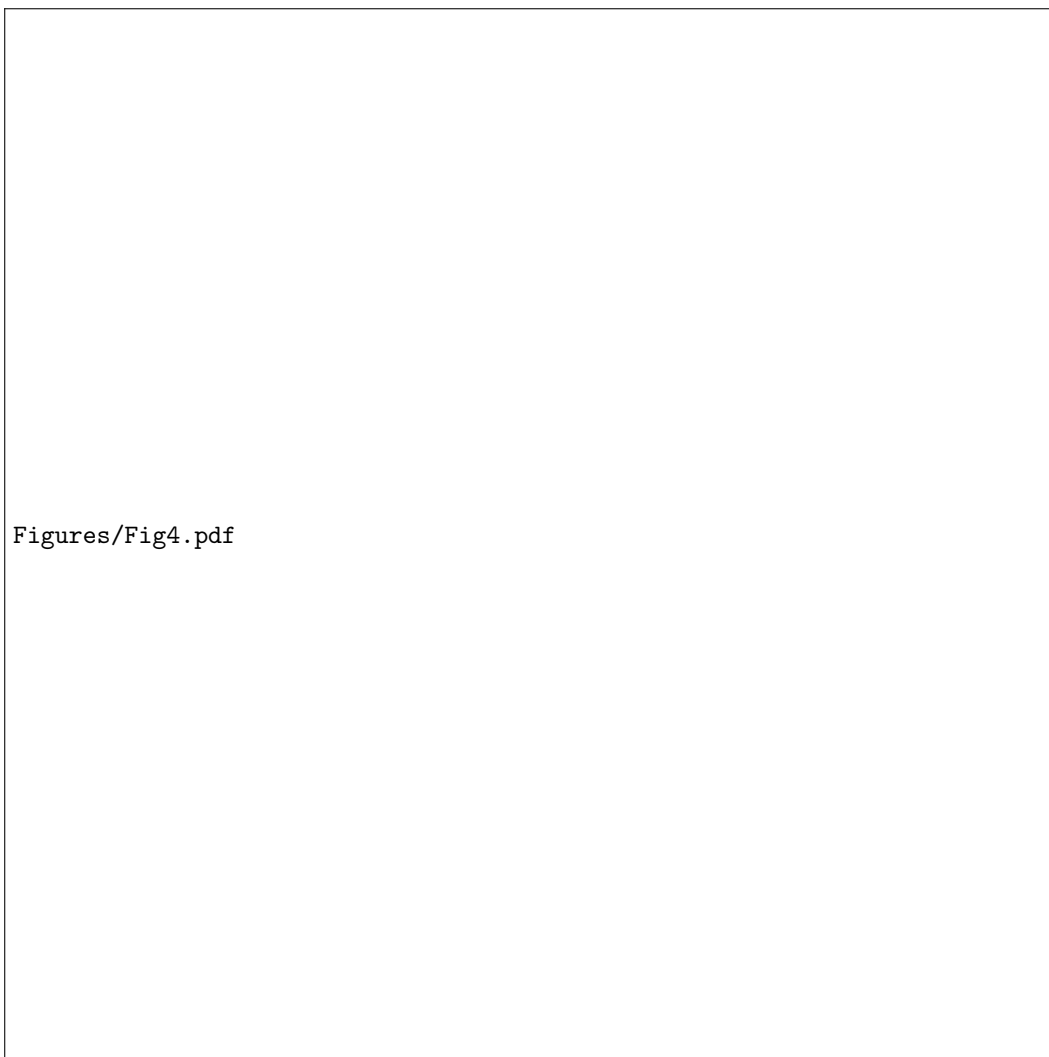


Figure 4. Result of the Monte-Carlo inversion. (a): Temperature rise as a function of time (black) together with the associated measurement uncertainty (gray) during the Sol 680-682 active heating experiment together with the best fit model (red). (b) Logarithmic time derivative of the temperature rise as a function of time (black) together with the best fit model (red). (c) Histogram of thermal conductivities for the models fitting the prescribed uncertainty within error bounds ($1\text{-}\sigma$, green) as well as histogram of models also fitting the constraint posed by the surface thermal inertia (TI, red). (d) Same as (c), but showing the histogram of admissible soil densities.

317 fits the data excellently, and the residual root mean square misfit is only 60 mK. The
 318 logarithmic time derivative of the data is shown together with the best fit model in panel
 319 (b), demonstrating that the model also fits the time derivative well on average. Histograms
 320 of admissible thermal conductivities are shown in Fig. 4(c), where the histogram for mod-
 321 els fitting the heating curve is shown in green ($1-\sigma$), while models satisfying the addi-
 322 tional constrain posed by the observed surface thermal inertia are shown in red. For the
 323 two cases considered, thermal conductivity is $k = 0.0395 \pm 0.0006$ and $k = 0.0395 \pm$
 324 $0.0008 \text{ W m}^{-1} \text{ K}^{-1}$, respectively. Overall, only a very small range of thermal conduc-
 325 tivities fits the data, allowing us to put tight constraints on the admissible values.

326 Histograms for the admissible soil density are shown in Fig. 4(d), and a large spread
 327 is visible in the range of admissible values. The Median density for models satisfying the
 328 heating curve constraint is 1007 kg m^{-3} and the 25th and 75th percentile are given by
 329 993 and 1184 kg m^{-3} , respectively, corresponding to an interquartile range or midspread
 330 of 191 kg m^{-3} . For models satisfying the additional constraint posed by the surface ther-
 331 mal inertia, the median density is 1211 kg m^{-3} with 25th and 75th percentiles of 1098
 332 and 1360 kg m^{-3} , corresponding to a midspread of 262 kg m^{-3} . Finally, contact con-
 333 ductances compatible with the available constrains have median contact conductances
 334 of 70 and $28 \text{ W m}^{-2} \text{ K}^{-1}$ for models satisfying the heating curve and the thermal in-
 335 ertia constraint, respectively (not shown). The 25th and 75th percentiles are 30 and 121
 336 $\text{W m}^{-2} \text{ K}^{-1}$ as well as 19 and $37 \text{ W m}^{-2} \text{ K}^{-1}$, respectively. For comparison, 10 W m^{-2}
 337 K^{-1} corresponds to the conductance across a 1 mm wide, CO_2 filled gap, whereas 2 W
 338 $\text{m}^{-2} \text{ K}^{-1}$ would correspond to purely radiative coupling at 220 K . Therefore, contact
 339 conductances needed to fit the data are reasonable.

340 4.2 Uncertainty Error Budget

341 The total measurement uncertainty for the determination of thermal conductiv-
 342 ity from HP³ active heating experiments was estimated by Grott et al. (2019) and found
 343 to be 3.7 %. However, it was assumed that the influence of the unknown soil density and
 344 contact conductance would be small due to the fact that the logarithmic time deriva-
 345 tive of the temperature rise at large times t could be used for the fitting. As this is not
 346 the case for the dataset considered here, the contributions of unknown soil density and
 347 contact conductance to the uncertainty budget need to be reassessed.

Error Source	Value [%]	Distr.	σ [%]	Remarks
Sensor Heat input	0.1	normal	0.1	Grott et al. (2019)
Soil density, thermal contact	2	normal	2	This paper
Modeling	4	uniform	2.3	Grott et al. (2019)
Reference method	2.5	normal	2.5	Grott et al. (2019)
Total 1σ Uncertainty			3.9	

Table 1. Error sources taken into account for determining the thermal conductivity uncertainty budget. Uncertainty, distribution function, as well as error contribution σ are given together with an indication of how the individual contributions were derived. Following the relevant standards (VIM, 2004; GUM, 2008), uniformly distributed uncertainties propagate into the total error budget weighted by one over the square root of three. Stated uncertainties are 1σ confidence limits.

348 Total measurement uncertainty for the determined thermal conductivity σ_k is given
 349 by Gaussian error propagation, and

$$\sigma_k = (\sigma_Q^2 + \sigma_{reg}^2 + \sigma_{mod}^2 + \sigma_{THS}^2)^{1/2} \quad (4)$$

350 Here, σ_Q is the uncertainty associated with determining the heat input into the TEM-
 351 A foils, σ_{reg} is the contribution stemming from the allowable spread of models determined
 352 using the Monte-Carlo simulations above, and σ_{mod} is the uncertainty associated with
 353 the imperfections of the finite element model representing the mole. The latter has been
 354 estimated during instrument calibration by a comparison with measurements in a low
 355 thermal conductivity granulate (Grott et al., 2019). Finally, σ_{THS} is the uncertainty of
 356 the reference measurement originally used to calibrate the finite element model (Ham-
 357 merschmidt & Sabuga, 2000). The numerical values of these contributions are summa-
 358 rized in Table 1, and a total $1\text{-}\sigma$ uncertainty of 3.9 % is obtained for the conductivity
 359 determined here. Given a best fit thermal conductivity of $0.039 \text{ W m}^{-1} \text{ K}^{-1}$, this cor-
 360 responds to an uncertainty of $\pm 0.002 \text{ W m}^{-1} \text{ K}^{-1}$.

4.3 Particle Size

Thermal conductivity determined from the active heating experiment can be interpreted in terms of soil grain size (e.g., Ferguson et al. (2006)) by a direct comparison with laboratory measurements under martian atmospheric conditions (Presley & Christensen, 1997; Presley & Craddock, 2006), and such estimates have been shown to be robust if the material is homogeneous and any indurated surface layers are much thinner than the diurnal skin depth (Edwards et al., 2018). Given soil thermal conductivity k in units of $[\text{W m}^{-1} \text{K}^{-1}]$, particle diameter d in units of $[\mu\text{m}]$ can be estimated from

$$d = \left(\frac{k}{CP^{0.6}} \right)^{-1/(0.11 \log(P/K))} \quad (5)$$

where P is atmospheric pressure in torr, and $C = 0.0015$ and $K = 8.1 \cdot 10^4$ are empirical fitting constants (Presley & Christensen, 1997). Eq. 5 is valid for thermal conductivities less than $0.1 \text{ m}^{-1} \text{K}^{-1}$, while larger conductivities are more difficult to interpret. Presley & Craddock (2006) have shown that the thermal conductivity of soils which include a variety of particle sizes is dominated by the largest grains, and Eq. 5 should provide a reasonable estimate of the size for which 85 to 95% of the particles are smaller than the size determined using the above equation. A thermal conductivity-derived particle size is therefore closer to a maximum particle size, rather than an average or modal size. Errors in deriving particle sizes with this method are expected to be less than 1015% (Presley & Christensen, 1997), provided cementation does not play a significant role.

Results of applying Eq. 5 to the thermal conductivity range of 0.01 to $0.05 \text{ W m}^{-1} \text{K}^{-1}$ (corresponding to thermal inertias of 100 to $240 \text{ J m}^{-2} \text{K}^{-1} \text{s}^{-1/2}$ assuming $\rho c_p = 10^6 \text{ J m}^{-3} \text{K}^{-1}$, Neugebauer et al. (1971)) are shown in Fig. 5, where particle diameter is shown as a function of thermal conductivity (solid line) together with a 15% uncertainty interval (gray). Grain sizes corresponding to a thermal conductivity of $0.039 \pm 0.002 \text{ W m}^{-1} \text{K}^{-1}$ are $136_{-32}^{+37} \mu\text{m}$, corresponding to very fine to fine cohesionless sand.

Images taken by the InSight Instrument Deployment Camera (IDC, Maki et al. (2018)) show that steep walls can be supported by the soil at the landing site. This indicates that the assumption of cohesionless sand may be an oversimplification. Rather, soil properties appear to be similar to those at the Phoenix landing site, for which trenches scraped by the robotic arm's scoop exhibited steep walls (Mellon et al., 2009). Overall, cohesion at the InSight landing site is estimated to be at least $1\text{-}1.9 \text{ kPa}$ (Golombek, Warner, et al., 2020), but may be as high as 14.5 kPa (Marteau et al., 2021), and the influence of

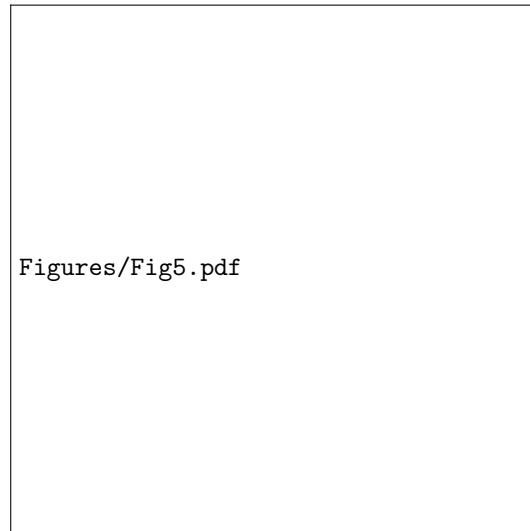


Figure 5. Particle diameter as a function of soil thermal conductivity according to the model of Presley & Christensen (1997) (black). The estimated 15% particle size uncertainty of the model is indicated in shades. The grain size derived from the thermal conductivity determined here is indicated in red, while the grain size derived assuming 0.02 vol% of cement forming necks between particles is indicated in yellow. For reference, the thermal inertia corresponding to the considered thermal conductivities assuming $\rho c_p = 10^6 \text{ J m}^{-3} \text{ K}^{-1}$ (Neugebauer et al., 1971) is also given.

392 cementation by, e.g., clays, carbonates, and chloride bearing minerals and salts (see Piqueux
393 & Christensen (2009b) and references therein) should also be considered.

394 Depending on the distribution of cementing agents, already tiny amounts of cement
395 can increase inter-grain contact and thus thermal conductivity. Assuming cement to pri-
396 marily form pendular rings at necks between grains, already 0.02 vol% of cement would
397 increase thermal conductivity by a factor of two according to the model of Piqueux &
398 Christensen (2009b). Using Eq. 5, this reduction in the underlying conductivity from
399 values of around $0.04 \text{ W m}^{-1} \text{ K}^{-1}$ to $0.02 \text{ W m}^{-1} \text{ K}^{-1}$ would correspond to grain sizes
400 of $30_{-7}^{+8} \mu\text{m}$ (see Fig. 5). Therefore, lightly cemented dust-sized particles would also be
401 consistent with the thermal properties determined here.

402 5 Summary and Discussion

403 The heat flow and physical properties package (HP³) of the InSight Mars mission
404 has conducted direct thermal conductivity measurements of martian soil. After initial
405 problems with inserting the probe into the soil, the mole was fully buried and a tip depth
406 of 0.37 m was reached. The active heating experiment was carried out on Sols 680 to 682
407 of the mission, and average thermal conductivity in the 0.03 to 0.37 m depth range was
408 found to be $0.039 \pm 0.002 \text{ W m}^{-1} \text{ K}^{-1}$. In addition, median soil density was constrained
409 to values of $1007_{-74}^{+176} \text{ kg m}^{-3}$ using Monte-Carlo simulations. Assuming that soil den-
410 sity, heat capacity, and thermal conductivity in the investigated depth range are sim-
411 ilar to those in the upper few centimeters of the soil, the range of admissible thermal in-
412 ertia determined by Golombek, Warner, et al. (2020) further constrains the soil density
413 to a median value of $1211_{-113}^{+149} \text{ kg m}^{-3}$.

414 The numerical model employed to determine thermal conductivity uses cylindri-
415 cal symmetry, while the mole was inclined at an angle of 30° with respect to vertical.
416 Therefore, a 3-dimensional model would in principle be needed, but since the distance
417 probed by the heat pulse is only a few centimeters (compare Fig. 3), the surroundings
418 of the mole can be assumed to be homogeneous to a good approximation. Therefore, the
419 influence of deviations from the ideal cylindrical symmetry is considered to be small.

420 As is evident from the history of probe emplacement (Sec. 2), some caution is needed
421 when interpreting the results, as the mechanical configuration of part of the sampled soil
422 may have been perturbed in the emplacement process (also see Marshall et al. (2017)).

423 Soil around the mole is likely compacted to an unknown degree, such that strictly speak-
 424 ing the thermal conductivity values reported here need to be considered as upper lim-
 425 its. One method to quantify the influence of compaction would be to independently es-
 426 timate thermal diffusivity from the amplitude of the diurnal temperature wave measured
 427 at the mole, but such an analysis is beyond the scope of this paper.

428 Thermal conductivity of the soil is expected to be temperature dependent (Mor-
 429 gan et al., 2018). Therefore, it would have been preferable to use less heating power and
 430 stimulate a smaller temperature response during the experiment, but this needed to be
 431 balanced against the desire to obtain a good signal to noise compared to the background
 432 temperature fluctuations. Therefore, it was decided to run the experiment using a heat-
 433 ing power of 2 W, inducing a temperature rise of 37.3 K. This may have increased the
 434 measured thermal conductivity by up to 8 % as compare to a measurement at the back-
 435 ground temperature (Morgan et al., 2018).

436 Thermal conductivity values determined here are more than a factor of two smaller
 437 than those determined with the TECP instrument on the Phoenix Mars mission (Zent
 438 et al., 2010), for which a thermal conductivity of $0.085 \text{ W m}^{-1} \text{ K}^{-1}$ was determined for
 439 the upper few centimeters of the soil. This may not be surprising given the presence of
 440 near surface ground ice as well as the abundant presence of cementing agents like per-
 441 chlorate salts at the polar Phoenix landing site (Hecht et al., 2009; Kounaves et al., 2014).
 442 However, overall even $0.085 \text{ W m}^{-1} \text{ K}^{-1}$ is relatively small, and both values indicate that
 443 the martian soil is a good thermal insulator. Furthermore, both values fall within the
 444 expected conductivity range for uncemented martian soils, which is 0.02 to 0.1 W m^{-1}
 445 K^{-1} (Grott et al., 2007).

446 As discussed in Sec. 4.3, the presence of cement can have a large influence on ther-
 447 mal conductivity. If present in the form of cementing necks, increased grain-to-grain con-
 448 tact areas will significantly increase thermal conductivity (Piqueux & Christensen, 2009b),
 449 and already 0.02 vol% of cement would increase thermal conductivity by a factor of two.
 450 As discussed, this would imply dust sized particles to be present. However, such small
 451 particle sizes seem to be implausible, as Homestead hollow appears to be filled by eo-
 452 lian deposits (Grant et al., 2020; Weitz et al., 2020) and the saltation limit for particles
 453 that can be mobilized by winds is 100 to 600 μm (Kok et al., 2012). Therefore, it seems
 454 more likely that cement present in the soil acts to increase cohesion but has only a small

455 influence on grain-to-grain contact areas. This could for example be the case if cement
456 is distributed in the form of grain coatings rather than cementing necks (Piqueux & Chris-
457 tensen, 2009b). In this case, thermal conductivity would increase linearly as a function
458 of volumetric cement content (Martinez, Alejandro et al., 2020) rather than the very steep
459 increase expected for deposition at particle contacts only (Piqueux & Christensen, 2009b).

460 Whether cement deposition in the form of particle coatings is sufficient to provide
461 the soil cohesion necessary to create clods and to support steep walls remains to be in-
462 vestigated. At the InSight landing site, cohesion of at least 1-1.9 kPa is required (Golombek,
463 Warner, et al., 2020), but may be as high as 14 kPa (Marteau et al., 2021). Lower bounds
464 on cohesion are similar to values found for crusty to cloddy soil at other landing sites
465 (0-4 kPa), whereas upper limits are similar to cohesion estimates for blocky, indurated
466 soil (3-11 kPa, see Golombek et al. (2008), Herkenhoff et al. (2008) and references therein).
467 Cohesion values determined at InSight are comparable to or higher than the 0.2 ± 0.4 kPa
468 to 1.2 ± 1.8 kPa derived from trenching experiments at the Phoenix landing site (Shaw
469 et al., 2009). Considering that perchlorate is present at a level of 0.6 wt% at the Phoenix
470 site (Hecht et al., 2009; Kounaves et al., 2014), similar amounts of cement could be present
471 at InSight. However, these would need to be distributed in the form of particle coatings
472 to be compatible with the thermal constraints discussed above.

473 The underlying particle-scale process that provides the cohesive strength of the soil
474 at the InSight landing site is not known. Nonetheless, it is likely a combination of inter-
475 particle bonding by cementation, electrostatic attraction due to surface tension, and in-
476 terlocking of the particles. In particular, a broad particle size distribution allows par-
477 ticles to interlock, providing mechanical bonds to create a supporting network which re-
478 tains large pore spaces. Moreover, it was found in laboratory studies that low environ-
479 mental pressure or hard vacuum result in a significant increase in cohesion of sands (Bromwell,
480 1966), which may help to explain the high cohesion apparent in the InSight images. Nev-
481 ertheless, if soil cohesion is closer to the upper limit of 14 kPa (Marteau et al., 2021),
482 these mechanisms may not be sufficient and particle cementation may be required to pro-
483 vide the necessary bonding.

484 In the light of the above discussion, grain size estimates based on a comparison with
485 laboratory experiments of essentially cohesionless sand need to be interpreted with cau-
486 tion. Also, it has to be kept in mind that the derived grain sizes are representative of

487 the larger particles in the mixture, with 85 to 95% of particles being smaller. Therefore,
 488 a significant amount of smaller, dust sized particles could be present, increasing soil co-
 489hesion and potentially explaining the presence of steep walls and clods. As the influence
 490of cohesion on thermal conductivity remains poorly constrained, estimates of particle size
 491remain uncertain. However, it seems likely that 85 to 95% of all particles are smaller than
 492104-173 μm based on a comparison with laboratory experiments (Presley & Christensen,
 4931997) and the fact that the investigated soil appears to be an eolian deposit (Grant et
 494al., 2020; Weitz et al., 2020).

495 Average soil thermal conductivity in the 0.03 to 0.37 m depth range determined
 496here is very similar to that derived from surface thermal inertia measurements using the
 497HP³ radiometer (Mueller et al., 2020). While a thin low conductivity layer of thickness
 498below 4 mm is required to explain the surface temperature response to solar eclipses by
 499the martian moon Phobos (Mueller et al., 2021), diurnal surface temperatures sensitive
 500to the upper $\sim 0.04\text{-}0.08$ m of the soil are consistent with a thermal conductivity of $0.041 \pm$
 501 $0.013 \text{ W m}^{-1} \text{ K}^{-1}$ (Piqueux et al., 2021). Therefore, the thermal data suggest that the
 502soil is largely homogeneous to a depth of 0.37 m.

503 Soil densities compatible with the temperature data are $1210_{-102}^{+219} \text{ kg m}^{-3}$ if soil prop-
 504erties in the 0.03 to 0.37 m depth range are assumed to be similar to those derived from
 505surface thermal inertia measurements (Golombek, Warner, et al., 2020). This falls within
 506the range of density estimates for other martian landing sites with crusty to cloddy soils,
 507for which values between 1100 to 1600 kg m^{-3} have been reported (Golombek et al., 2008).
 508Furthermore, the range of admissible densities determined here is compatible with pre-
 509landing estimates of 1300 kg m^{-3} (Morgan et al., 2018). These estimates of soil density
 510can be converted to an estimate of bulk porosity if the density of the constituent par-
 511ticles is assumed to be known. Here we assume particle density to be similar to that found
 512for basaltic martian meteorites, which have densities of 3100 to 3400 kg m^{-3} (Coulson
 513et al., 2007; Britt et al., 2012). Furthermore, petrological modeling indicates densities
 514of 3100 kg m^{-3} (Baratoux et al., 2014), such that the median densities derived above
 515would correspond to a bulk porosity of $\sim 61\%$. While this may appear large, it is quite
 516consistent with results obtained at the Phoenix landing site (55 %, Zent et al. (2010))
 517as well as the fact that mole hammering created a significant hole by compacting void
 518spaces during the early phases of probe insertion.

519 Experimental results on thermal conductivity as a function of porosity for various
 520 extra-terrestrial soil simulants under terrestrial atmospheric conditions are summarized
 521 by Becker & Vrettos (2016). Of the materials tested, three sands show grain-size char-
 522 acteristics similar to the soil encountered at the InSight landing site. These poorly-graded
 523 sands with mean grain sizes between 0.2 and 0.3 mm exhibit a thermal conductivity around
 524 $0.2 \text{ W m}^{-1} \text{ K}^{-1}$ at a typical porosity of 50%. In order to extrapolate conductivity to Mar-
 525 tian atmospheric conditions we scale the gas contribution to the conductivity to 20-25%
 526 of the terrestrial value as suggested by the results of Huetter et al. (2008). Adopting the
 527 analytical model by Haigh (2012) for the extrapolation, we obtain a proportional reduc-
 528 tion of the terrestrial conductivity value, resulting in predicted thermal conductivities
 529 close to $0.04\text{-}0.05 \text{ W m}^{-1} \text{ K}^{-1}$ under martian atmospheric conditions. This indicates that
 530 high porosities are compatible with the thermal properties determined above.

531 If radiometrically derived surface thermal inertia is not used as an additional con-
 532 straint, soil density estimates are reduced to $1007_{-74}^{+176} \text{ kg m}^{-3}$, and resulting porosity
 533 estimates would increase to 68 %. However, there are no strong indications of changing
 534 soil parameters in the depth range investigated here (Golombek, Warner, et al., 2020),
 535 and the constantly slow progress of the mole also argues for a rather homogeneous soil
 536 column. Therefore, the larger density estimates of $1211_{-113}^{+149} \text{ kg m}^{-3}$ appear to
 537 be more appropriate. Note, however, that it has been argued that a transition to cohe-
 538 sionless sand may be present at a depth of 0.2 m (Hudson et al., 2020), but this is dif-
 539 ficult to reconcile with the apparent similarity of thermal properties derived from radio-
 540 metric measurements (Piqueux et al., 2021) and the results presented here.

541 The thermal conductivity measured here falls within the range of predictions used
 542 for designing the HP³ instrument (Grott et al., 2007; Spohn et al., 2018), which was 0.02
 543 to $0.1 \text{ W m}^{-1} \text{ K}^{-1}$. Based on the measurement of soil thermal conductivity at the In-
 544 Sight landing site and assuming heat flow to be 19 to 24 mW m^{-2} (Plesa, Grott, Tosi,
 545 et al., 2016), the subsurface thermal gradient is expected to be 0.45 to 0.64 K m^{-1} . This
 546 is well above the design limit of 0.2 K m^{-1} to guarantee an overall 1- σ heat flow uncer-
 547 tainty of 2.2 mW m^{-2} (Spohn et al., 2018). The relatively low thermal conductivity of
 548 $0.039 \pm 0.002 \text{ W m}^{-1} \text{ K}^{-1}$ further reduces the influence of perturbations to the subsur-
 549 face heat flow, which can be caused by, e.g., the InSight lander (Grott, 2009; Siegler et
 550 al., 2017), interannual variations of surface temperature (Grott et al., 2007), as well as
 551 surface temperature changes induced by martian dust storms (Plesa, Grott, Lemmon,

552 et al., 2016). The thermal conductivity determined here will therefore help to design fu-
 553 ture heat flow probes by providing important constraints on the thermophysical prop-
 554 erties of the martian soil.

555 Soil thermal conductivities derived here and those derived from radiometric mea-
 556 surements of surface brightness temperatures (Piqueux et al., 2021) place strong con-
 557 straints on the allowable degree of soil cementation. However, these results are difficult
 558 to reconcile with the analysis of image data, which strongly suggests an indurated duri-
 559 crust to be present (Golombek, Warner, et al., 2020), as well as the analysis of soil me-
 560 chanical properties, which argues for soil cohesion in the 2 to 14 kPa range (Marteau et
 561 al., 2021). When compared to other martian landing sites, thermal properties are thus
 562 similar to those of crusty to cloddy soils (thermal inertia of 200 to 326 J m⁻² K⁻¹ s^{-1/2},
 563 cohesion of 0 to 4 kPa), while mechanical properties are more consistent with blocky to
 564 indurated soils (thermal inertia of 368 to 410 J m⁻² K⁻¹ s^{-1/2}, cohesion of 3 to 11 kPa,
 565 Golombek et al. (2008)). This apparent discrepancy between the interpretation of the
 566 thermal and mechanical properties cannot be resolved here and certainly deserves fur-
 567 ther study.

568 **Acknowledgments**

569 The design, building of and research into the HP³ has been supported by the German
 570 Aerospace Center DLR, by NASA, the AW, and the Polish Academy of Science. The nu-
 571 merical code and data necessary to reproduce the results of this paper have been made
 572 publicly available in Grott (2021). Part of this work was performed at the Jet Propul-
 573 sion Laboratory, California Institute of Technology, under a contract with NASA. US
 574 government support is gratefully acknowledged. This paper is InSight Contribution Num-
 575 ber 210.

576 **References**

- 577 Banerdt, W. B., Smrekar, S. E., Banfield, D., Giardini, D., Golombek, M., Johnson,
 578 C. L., ... Wiczorek, M. (2020). Initial results from the InSight mission on Mars.
 579 *Nature Geoscience*, 13(3), 183-189. doi: 10.1038/s41561-020-0544-y
- 580 Banin, A., Clark, B. C., & Waenke, H. (1992). Surface chemistry and mineralogy. In
 581 M. George (Ed.), *Mars* (p. 594-625).
- 582 Baratoux, D., Samuel, H., Michaut, C., Toplis, M. J., Monnereau, M., Wiczorek,

- 583 M., ... Kurita, K. (2014). Petrological constraints on the density of the Mar-
 584 tian crust. *Journal of Geophysical Research (Planets)*, 119(7), 1707-1727. doi:
 585 10.1002/2014JE004642
- 586 Becker, A., & Vrettos, C. (2016). Tests on the thermal conductivity of regolith
 587 quasi-analogues at different porosities. In *Earth and space 2016* (p. 9-15). doi: 10
 588 .1061/9780784479971.002
- 589 Britt, D. T., Macke, R. J., Kiefer, W. S., Irving, A. J., Hupé, G., & Consolmagno,
 590 G. J. (2012). The Density, Porosity, and Magnetic Susceptibility of Two Recent
 591 Meteorite Falls: Tissint and Sutter's Mill. *Meteoritics and Planetary Science*
 592 *Supplement*, 75, 5350.
- 593 Bromwell, L. G. (1966). *The friction of quartz in high vacuum* (Tech. Rep. No. 3-
 594 101). Department of Civil Engineering, M.I.T. Cambridge, MA: Research In Earth
 595 Physics, Phase Report No. 7.
- 596 Christensen, P. R., & Moore, H. J. (1992). The martian surface layer. In M. George
 597 (Ed.), *Mars* (p. 686-729).
- 598 Coulson, I. M., Beech, M., & Nie, W. (2007). Physical properties of Martian me-
 599 teorites: Porosity and density measurements. *Meteoritics and Planetary Science*,
 600 42(12), 2043-2054. doi: 10.1111/j.1945-5100.2007.tb01006.x
- 601 Ditteon, R. (1982). Daily temperature variations on Mars. *Journal of Geophysical*
 602 *Research*, 87, 10197-10214. doi: 10.1029/JB087iB12p10197
- 603 Edgett, K. S., Yingst, R. A., Minitti, M. E., Goetz, W., Kah, L. C., Kennedy,
 604 M. R., ... MSL Science Team (2013, March). Mars Hand Lens Imager (MAHLI)
 605 Efforts and Observations at the "Rocknest" Eolian Sand Shadow in Curiosity's
 606 Gale Crater Field Site. In *Lunar and planetary science conference* (p. 1201).
- 607 Edwards, C. S., Piqueux, S., Hamilton, V. E., Fergason, R. L., Herkenhoff, K. E.,
 608 Vasavada, A. R., ... Smith, M. D. (2018). The Thermophysical Properties of the
 609 Bagnold Dunes, Mars: Ground-Truthing Orbital Data. *Journal of Geophysical*
 610 *Research (Planets)*, 123(5), 1307-1326. doi: 10.1029/2017JE005501
- 611 Fergason, R., Christensen, P., Bell, J., Golombek, M., Herkenhoff, K., & Kieffer,
 612 H. (2006). Physical properties of the Mars Exploration Rover landing sites as
 613 inferred from Mini-TES-derived thermal inertia. *Journal of Geophysical Research*
 614 *(Planets)*, 111(E2), E02S21. doi: 10.1029/2005JE002583
- 615 Golombek, M., Grott, M., Kargl, G., Andrade, J., Marshall, J., Warner, N., ...

- 616 Banerdt, W. B. (2018). Geology and Physical Properties Investigations
 617 by the InSight Lander. *Space Science Reviews*, 214(5), 84. doi: 10.1007/
 618 s11214-018-0512-7
- 619 Golombek, M., Haldemann, A. F. C., Simpson, R. A., Fergason, R. L., Putzig, N. E.,
 620 Arvidson, R. E., ... Mellon, M. T. (2008). Martian surface properties from joint
 621 analysis of orbital, Earth-based, and surface observations. In I. Bell Jim (Ed.),
 622 *The martian surface - composition, mineralogy, and physical properties* (p. 468).
- 623 Golombek, M., Kass, D., Williams, N., Warner, N., Daubar, I., Piqueux, S., ...
 624 Pike, W. T. (2020). Assessment of InSight Landing Site Predictions. *Journal of*
 625 *Geophysical Research (Planets)*, 125(8), e06502. doi: 10.1029/2020JE006502
- 626 Golombek, M., Kipp, D., Warner, N., Daubar, I. J., Fergason, R., Kirk, R. L., ...
 627 Banerdt, W. B. (2017). Selection of the InSight Landing Site. *Space Science*
 628 *Reviews*, 211(1-4), 5-95. doi: 10.1007/s11214-016-0321-9
- 629 Golombek, M., Warner, N. H., Grant, J. A., Hauber, E., Ansan, V., Weitz, C. M.,
 630 ... Banerdt, W. B. (2020). Geology of the InSight landing site on Mars. *Nature*
 631 *Communications*, 11, 1014. doi: 10.1038/s41467-020-14679-1
- 632 Golombek, M., Williams, N., Warner, N. H., Parker, T., Williams, M. G., Daubar,
 633 I., ... Sklyanskiy, E. (2020). Location and Setting of the Mars InSight Lander,
 634 Instruments, and Landing Site. *Earth and Space Science*, 7(10), e01248. doi:
 635 10.1029/2020EA001248
- 636 Gómez-Elvira, J., Armiens, C., Castañer, L., Domínguez, M., Genzer, M., Gómez,
 637 F., ... Martín-Torres, J. (2012). REMS: The Environmental Sensor Suite for the
 638 Mars Science Laboratory Rover. *Space Science Reviews*, 170(1-4), 583-640. doi:
 639 10.1007/s11214-012-9921-1
- 640 Grant, J. A., Warner, N. H., Weitz, C. M., Golombek, M. P., Wilson, S. A., Baker,
 641 M., ... Banks, M. E. (2020). Degradation of Homestead Hollow at the InSight
 642 Landing Site Based on the Distribution and Properties of Local Deposits. *Journal*
 643 *of Geophysical Research (Planets)*, 125(4), e06350. doi: 10.1029/2019JE006350
- 644 Grott, M. (2009). Thermal disturbances caused by lander shadowing and the mea-
 645 surability of the martian planetary heat flow. *Planetary and Space Science*, 57(1),
 646 71-77. doi: 10.1016/j.pss.2008.11.005
- 647 Grott, M. (2021). Supplementary Material for "Thermal Conductivity of the Mar-
 648 tian Regolith at the InSight Landing site from HP³ Active Heating Experiments".

- 649 *Figshare*. doi: <https://doi.org/10.6084/m9.figshare.c.5255468>
- 650 Grott, M., Helbert, J., & Nadalini, R. (2007). Thermal structure of Martian soil
651 and the measurability of the planetary heat flow. *Journal of Geophysical Research*
652 *(Planets)*, *112*(E9), E09004. doi: 10.1029/2007JE002905
- 653 Grott, M., Knollenberg, J., & Krause, C. (2010). Apollo lunar heat flow experiment
654 revisited: A critical reassessment of the in situ thermal conductivity determi-
655 nation. *Journal of Geophysical Research (Planets)*, *115*(E11), E11005. doi:
656 10.1029/2010JE003612
- 657 Grott, M., Spohn, T., Knollenberg, J., Krause, C., Scharringhausen, M., Wipper-
658 mann, T., ... Banerdt, W. B. (2019). Calibration of the Heat Flow and Physical
659 Properties Package (HP³) for the InSight Mars Mission. *Earth and Space Science*,
660 *6*(12), 2556-2574. doi: 10.1029/2019EA000670
- 661 GUM. (2008). *Evaluation of measurement data Guide to the expression of uncer-*
662 *tainty in measurement*. Joint Committee for Guides in Metrology.
- 663 Haigh, S. (2012). Thermal conductivity of sands. *Geotechnique*, *62*(7), 617-625. doi:
664 10.1680/geot.11.P.043
- 665 Hamilton, V. E., Vasavada, A. R., Sebastián, E., Torre Juárez, M., Ramos, M.,
666 Armiens, C., ... Zorzano, M.-P. (2014). Observations and preliminary science
667 results from the first 100 sols of MSL Rover Environmental Monitoring Station
668 ground temperature sensor measurements at Gale Crater. *Journal of Geophysical*
669 *Research (Planets)*, *119*(4), 745-770. doi: 10.1002/2013JE004520
- 670 Hammerschmidt, U., & Sabuga, W. (2000). Transient hot wire (THW) method: Un-
671 certainty Assessment. *Intern. J. Thermophys.*, *21*(6), 1225-1278.
- 672 Haskin, L. A., Wang, A., Jolliff, B. L., McSween, H. Y., Clark, B. C., Des Marais,
673 D. J., ... Soderblom, L. (2005). Water alteration of rocks and soils on
674 Mars at the Spirit rover site in Gusev crater. *Nature*, *436*(7047), 66-69. doi:
675 10.1038/nature03640
- 676 Hecht, M. H., Kounaves, S. P., Quinn, R. C., West, S. J., Young, S. M. M., Ming,
677 D. W., ... Smith, P. H. (2009). Detection of Perchlorate and the Soluble Chem-
678 istry of Martian Soil at the Phoenix Lander Site. *Science*, *325*(5936), 64. doi:
679 10.1126/science.1172466
- 680 Herkenhoff, K. E., Golombek, M. P., Guinness, E. A., Johnson, J. B., Kusack, A.,
681 Richter, L., ... Gorevan, S. (2008). In situ observations of the physical properties

- 682 of the Martian surface. In I. Bell Jim (Ed.), *The martian surface - composition,*
683 *mineralogy, and physical properties* (p. 451).
- 684 Hudson, T. L., Deen, R., Marteau, E., Golombek, M., Hurst, K., Spohn, T., . . .
685 Knollenberg, J. (2020, March). InSight HP3 Mole Near-Surface Motion and
686 Subsurface Implications. In *Lunar and planetary science conference* (p. 1217).
- 687 Huetter, E. S., Koemle, N. I., Kargl, G., & Kaufmann, E. (2008, December). De-
688 termination of the effective thermal conductivity of granular materials under
689 varying pressure conditions. *Journal of Geophysical Research (Planets)*, *113*(E12),
690 E12004. doi: 10.1029/2008JE003085
- 691 Hurowitz, J. A., McLennan, S. M., Tosca, N. J., Arvidson, R. E., Michalski, J. R.,
692 Ming, D. W., . . . Squyres, S. W. (2006). In situ and experimental evidence for
693 acidic weathering of rocks and soils on Mars. *Journal of Geophysical Research*
694 *(Planets)*, *111*(E2), E02S19. doi: 10.1029/2005JE002515
- 695 Jaeger, J. C. (1956). Conduction of Heat in an Infinite Region Bounded Internally
696 by a Circular Cylinder of a Perfect Conductor. *Australian Journal of Physics*, *9*,
697 167. doi: 10.1071/PH560167
- 698 Jakosky, B. M., & Christensen, P. R. (1986). Are the Viking Lander sites represen-
699 tative of the surface of Mars? *Icarus*, *66*(1), 125-133. doi: 10.1016/0019-1035(86)
700 90012-6
- 701 Kieffer, H. H., Martin, T. Z., Peterfreund, A. R., Jakosky, B. M., Miner, E. D., &
702 Palluconi, F. D. (1977). Thermal and albedo mapping of Mars during the Viking
703 primary mission. *Journal of Geophysical Research*, *82*(B28), 4249-4292. doi:
704 10.1029/JS082i028p04249
- 705 Kok, J. F., Parteli, E. J. R., Michaels, T. I., & Karam, D. B. (2012). The physics of
706 wind-blown sand and dust. *Reports on Progress in Physics*, *75*(10), 106901. doi:
707 10.1088/0034-4885/75/10/106901
- 708 Kounaves, S. P., Chaniotakis, N. A., Chevrier, V. F., Carrier, B. L., Folds, K. E.,
709 Hansen, V. M., . . . Weber, A. W. (2014). Identification of the perchlorate parent
710 salts at the Phoenix Mars landing site and possible implications. *Icarus*, *232*,
711 226-231. doi: 10.1016/j.icarus.2014.01.016
- 712 Maki, J. N., Golombek, M., Deen, R., Abarca, H., Sorice, C., Goodsall, T., . . .
713 Banerdt, W. B. (2018, September). The Color Cameras on the InSight Lander.
714 *Space Science Reviews*, *214*(6), 105. doi: 10.1007/s11214-018-0536-z

- 715 Marshall, J. P., Hudson, T. L., & Andrade, J. E. (2017). Experimental Investigation
716 of InSight HP³ Mole Interaction with Martian Regolith Simulant. Quasi-Static
717 and Dynamic Penetration Testing. *Space Science Reviews*, *211*(1-4), 239-258. doi:
718 10.1007/s11214-016-0329-1
- 719 Marteau, E., Golombek, M., Vrettos, C., & Garvin, J. (2021). Soil Mechanical Prop-
720 erties at the InSight Landing Site on Mars. In *Lunar and planetary science confer-*
721 *ence* (p. 2067).
- 722 Martinez, Alejandro, Huang, Lin, & Gomez, Michael G. (2020). Enhancement of the
723 thermal conductivity of sands via microbially-induced calcite precipitation. *E3S*
724 *Web Conf.*, *205*, 09011. doi: 10.1051/e3sconf/202020509011
- 725 Mellon, M. T., Arvidson, R. E., Sizemore, H. G., Searls, M. L., Blaney, D. L., Cull,
726 S., . . . Zent, A. P. (2009). Ground ice at the phoenix landing site: Stabil-
727 ity state and origin. *Journal of Geophysical Research: Planets*, *114*(E1). doi:
728 <https://doi.org/10.1029/2009JE003417>
- 729 Mellon, M. T., Jakosky, B. M., Kieffer, H. H., & Christensen, P. R. (2000). High-
730 Resolution Thermal Inertia Mapping from the Mars Global Surveyor Thermal
731 Emission Spectrometer. *Icarus*, *148*(2), 437-455. doi: 10.1006/icar.2000.6503
- 732 Moore, H. J., Bickler, D. B., Crisp, J. A., Eisen, H. J., Gensler, J. A., Haldemann,
733 A. F. C., . . . Pavlics, F. (1999). Soil-like deposits observed by Sojourner, the
734 Pathfinder rover. *Journal of Geophysical Research*, *104*(E4), 8729-8746. doi:
735 10.1029/1998JE900005
- 736 Morgan, P., Grott, M., Knapmeyer-Endrun, B., Golombek, M., Delage, P.,
737 Lognonné, P., . . . Kedar, S. (2018). A Pre-Landing Assessment of Regolith
738 Properties at the InSight Landing Site. *Space Science Reviews*, *214*(6), 104. doi:
739 10.1007/s11214-018-0537-y
- 740 Mueller, N. T., Knollenberg, J., Grott, M., Kopp, E., Walter, I., Krause, C., . . . Sm-
741 rekar, S. (2020). Calibration of the HP³ Radiometer on InSight. *Earth and Space*
742 *Science*, *7*(5), e01086. doi: 10.1029/2020EA001086
- 743 Mueller, N. T., Piqueux, S., Lemmon, M., Maki, J., Lorenz, R., Grott, M., . . .
744 Banerdt, W. (2021). Near surface properties derived from Phobos transits with
745 HP³ RAD on InSight, Mars. *Geophysical Research Letters*, *submitted*.
- 746 Mutch, T. A., Arvidson, R. E., Binder, A. B., Guinness, E. A., & Morris, E. C.
747 (1977). The geology of the Viking lander 2 site. *Journal of Geophysical Research*,

- 748 82(B28), 4452-4467. doi: 10.1029/JS082i028p04452
- 749 Neugebauer, G., Münch, G., Kieffer, H., Chase, J., S. C., & Miner, E. (1971).
 750 Mariner 1969 Infrared Radiometer Results: Temperatures and Thermal Properties
 751 of the Martian Surface. *Astronomical Journal*, 76, 719. doi: 10.1086/111189
- 752 Palluconi, F. D., & Kieffer, H. H. (1981). Thermal inertia mapping of Mars from 60S
 753 to 60N. *Icarus*, 45(2), 415-426. doi: 10.1016/0019-1035(81)90044-0
- 754 Piqueux, S., & Christensen, P. R. (2009a). A model of thermal conductivity for
 755 planetary soils: 1. Theory for unconsolidated soils. *Journal of Geophysical Re-*
 756 *search (Planets)*, 114(E9), E09005. doi: 10.1029/2008JE003308
- 757 Piqueux, S., & Christensen, P. R. (2009b). A model of thermal conductivity for
 758 planetary soils: 2. Theory for cemented soils. *Journal of Geophysical Research*
 759 *(Planets)*, 114(E9), E09006. doi: 10.1029/2008JE003309
- 760 Piqueux, S., Mueller, N., Grott, M., Siegler, M., Millour, E., Forget, F., ... Smrekar,
 761 W., S.E. Banerdt (2021). Regolith Properties near the InSight Lander Derived
 762 from 50 Sols of Radiometer Measurements. *Journal of Geophysical Research*
 763 *(Planets)*, submitted.
- 764 Plesa, A. C., Grott, M., Lemmon, M. T., Müller, N., Piqueux, S., Siegler, M. A., ...
 765 Spohn, T. (2016). Interannual perturbations of the Martian surface heat flow by
 766 atmospheric dust opacity variations. *Journal of Geophysical Research (Planets)*,
 767 121(10), 2166-2175. doi: 10.1002/2016JE005127
- 768 Plesa, A. C., Grott, M., Tosi, N., Breuer, D., Spohn, T., & Wieczorek, M. A.
 769 (2016). How large are present-day heat flux variations across the surface of
 770 Mars? *Journal of Geophysical Research (Planets)*, 121(12), 2386-2403. doi:
 771 10.1002/2016JE005126
- 772 Pollack, J. B., Colburn, D. S., Flasar, F. M., Kahn, R., Carlston, C. E., & Pi-
 773 dek, D. G. (1979). Properties and effects of dust particles suspended in the
 774 Martian atmosphere. *Journal of Geophysical Research*, 84, 2929-2945. doi:
 775 10.1029/JB084iB06p02929
- 776 Presley, M. A., & Christensen, P. R. (1997). The effect of bulk density and particle
 777 size sorting on the thermal conductivity of particulate materials under Martian
 778 atmospheric pressures. *Journal of Geophysical Research (Planets)*, 102(E4),
 779 9221-9230. doi: 10.1029/97JE00271
- 780 Presley, M. A., & Craddock, R. A. (2006). Thermal conductivity measurements of

- 781 particulate materials: 3. Natural samples and mixtures of particle sizes. *Journal of*
782 *Geophysical Research (Planets)*, 111(E9), E09013. doi: 10.1029/2006JE002706
- 783 Presley, M. A., Craddock, R. A., & Zolotova, N. (2009). The effect of salt crust on
784 the thermal conductivity of one sample of fluvial particulate materials under Mar-
785 tian atmospheric pressures. *Journal of Geophysical Research (Planets)*, 114(E11),
786 E11007. doi: 10.1029/2009JE003355
- 787 Putzig, N. E., & Mellon, M. T. (2007). Apparent thermal inertia and the surface
788 heterogeneity of Mars. *Icarus*, 191(1), 68-94. doi: 10.1016/j.icarus.2007.05.013
- 789 Shaw, A., Arvidson, R. E., Bonitz, R., Carsten, J., Keller, H. U., Lemmon, M. T.,
790 ... Trebi-Ollennu, A. (2009). Phoenix soil physical properties investigation.
791 *Journal of Geophysical Research: Planets*, 114(E1). doi: [https://doi.org/10.1029/](https://doi.org/10.1029/2009JE003455)
792 2009JE003455
- 793 Siegler, M. A., Smrekar, S. E., Grott, M., Piqueux, S., Mueller, N., Williams, J.-P.,
794 ... Spohn, T. (2017, October). The InSight Mars Lander and Its Effect on the
795 Subsurface Thermal Environment. *Space Science Reviews*, 211(1-4), 259-275. doi:
796 10.1007/s11214-017-0331-2
- 797 Spohn, T., Grott, M., Smrekar, S. E., Knollenberg, J., Hudson, T. L., Krause, C.,
798 ... Banerdt, W. B. (2018). The Heat Flow and Physical Properties Pack-
799 age (HP³) for the InSight Mission. *Space Science Reviews*, 214(5), 96. doi:
800 10.1007/s11214-018-0531-4
- 801 VIM. (2004). *International vocabulary of basic and general terms in metrology*. Inter-
802 national Organization for Standardization.
- 803 Warner, N. H., Golombek, M. P., Sweeney, J., Ferguson, R., Kirk, R., & Schwartz,
804 C. (2017). Near Surface Stratigraphy and Regolith Production in Southwest-
805 ern Elysium Planitia, Mars: Implications for Hesperian-Amazonian Terrains and
806 the InSight Lander Mission. *Space Science Reviews*, 211(1-4), 147-190. doi:
807 10.1007/s11214-017-0352-x
- 808 Weitz, C. M., Grant, J. A., Golombek, M. P., Warner, N. H., Hauber, E., Ansan, V.,
809 ... Kopp, M. (2020). Comparison of InSight Homestead Hollow to Hollows at the
810 Spirit Landing Site. *Journal of Geophysical Research (Planets)*, 125(7), e06435.
811 doi: 10.1029/2020JE006435
- 812 Yingst, R. A., Kah, L. C., Palucis, M., Williams, R. M. E., Garvin, J., Bridges,
813 J. C., ... Wiens, R. C. (2013). Characteristics of pebble- and cobble-sized clasts

814 along the Curiosity rover traverse from Bradbury Landing to Rocknest. *Journal of*
815 *Geophysical Research (Planets)*, 118(11), 2361-2380. doi: 10.1002/2013JE004435
816 Zent, A. P., Hecht, M. H., Cobos, D. R., Wood, S. E., Hudson, T. L., Milkovich,
817 S. M., ... Mellon, M. T. (2010). Initial results from the thermal and electri-
818 cal conductivity probe (TECP) on Phoenix. *Journal of Geophysical Research*
819 *(Planets)*, 115(2), E00E14. doi: 10.1029/2009JE003420

Figure 1.

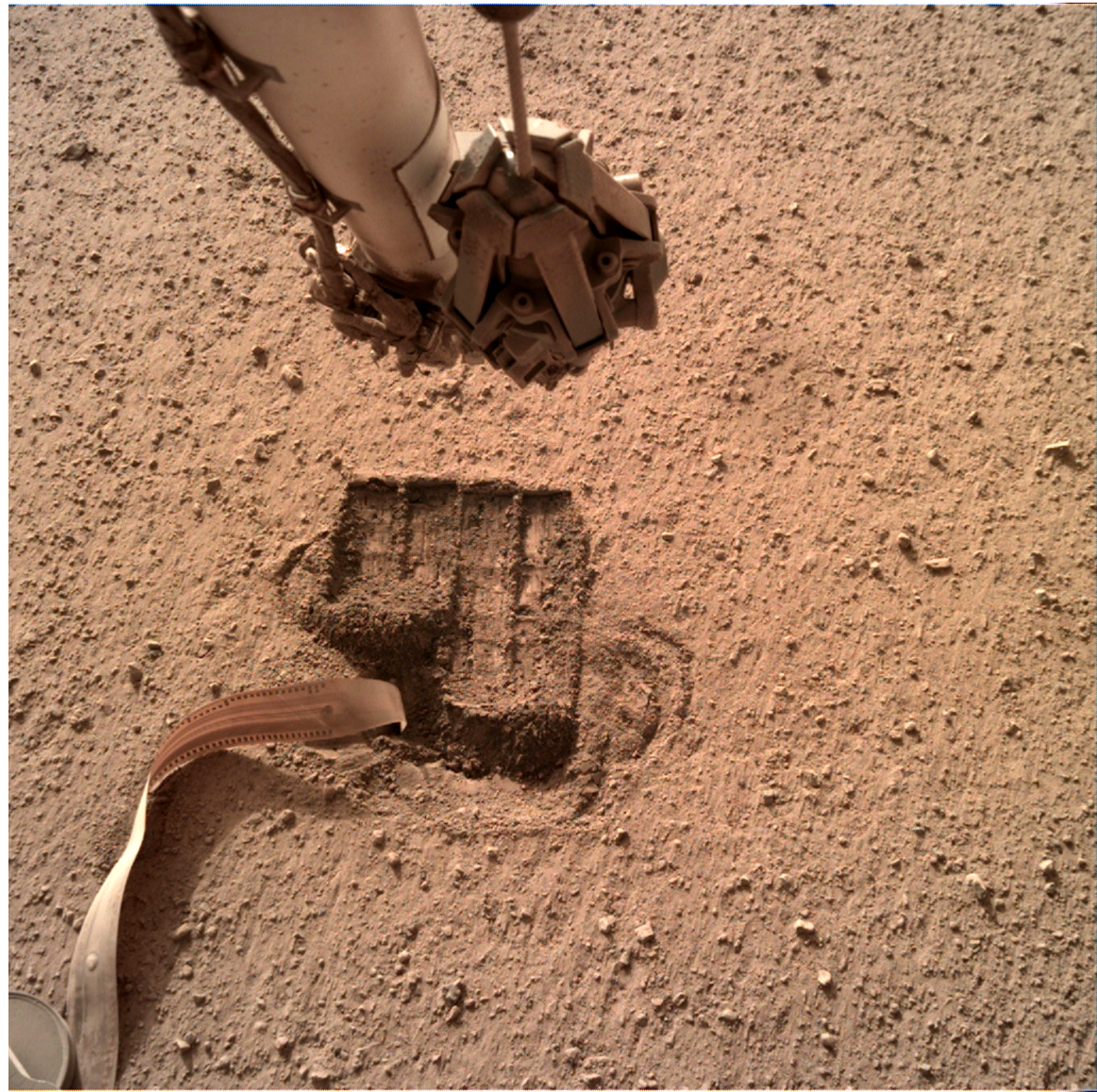
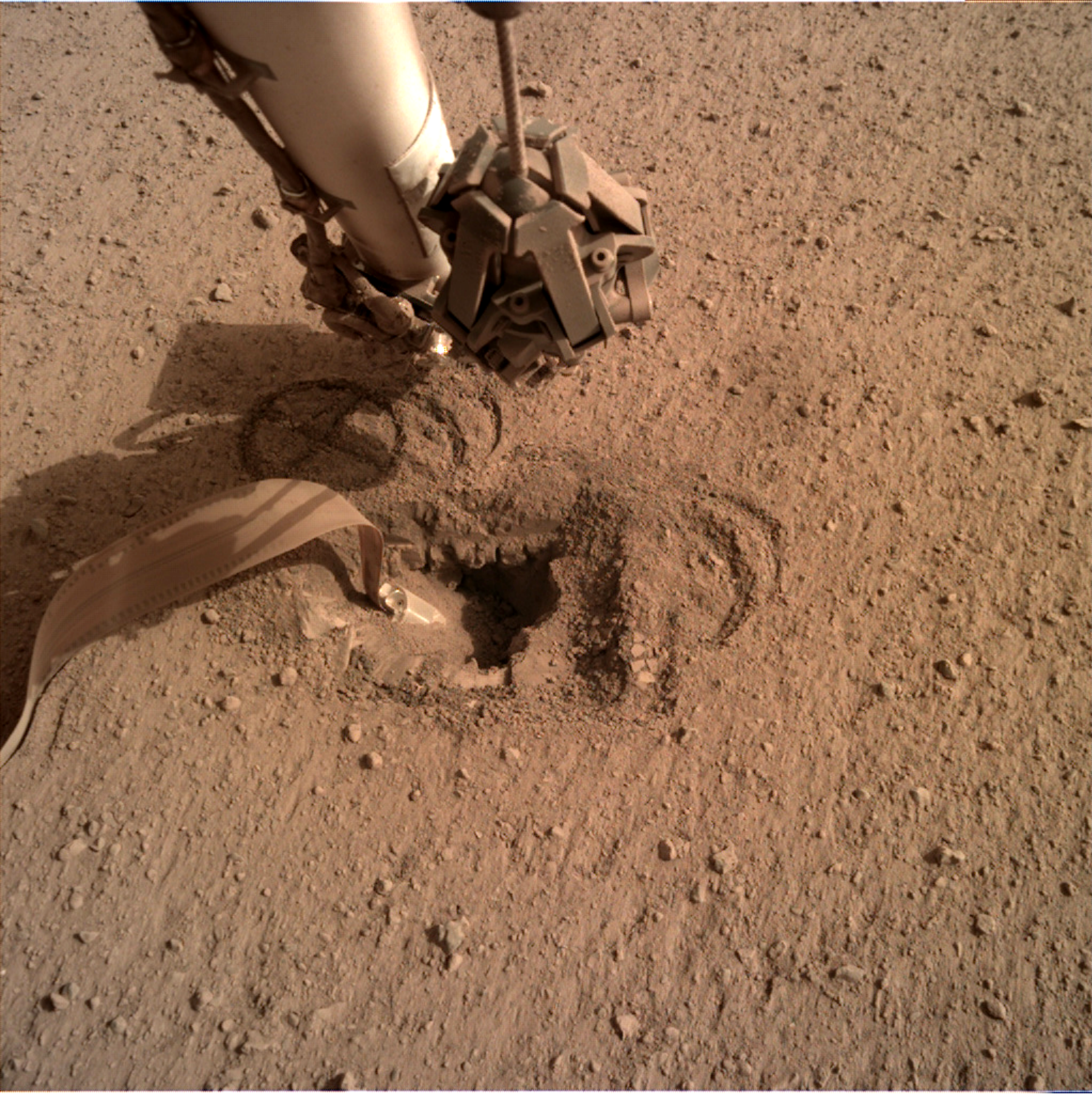


Figure 2.

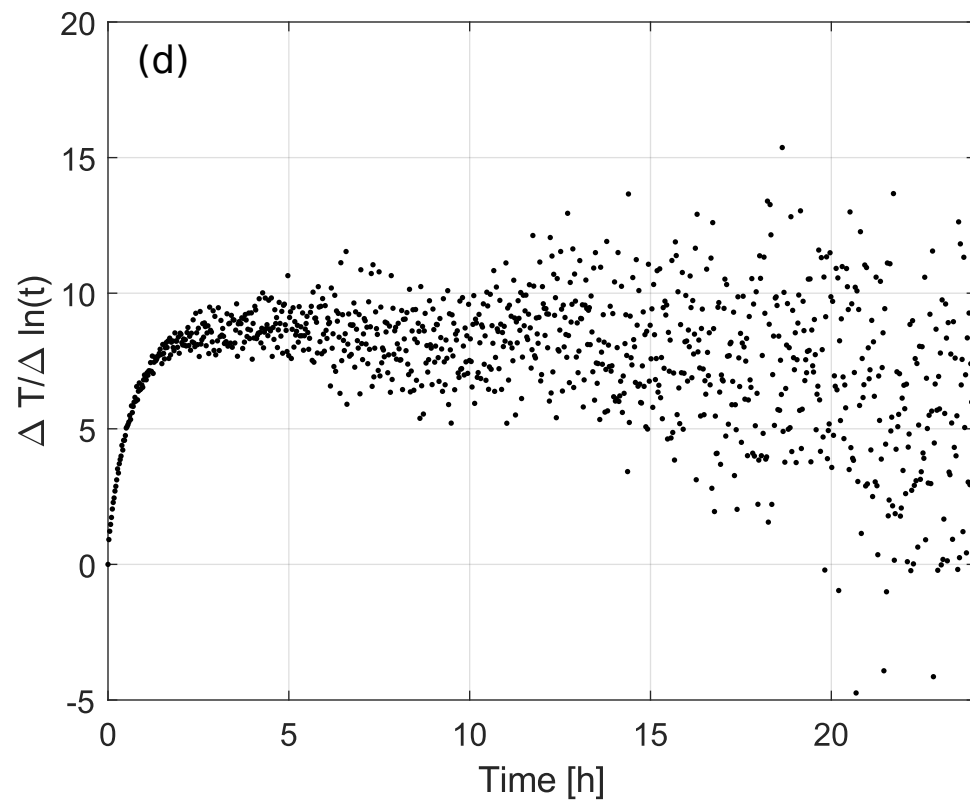
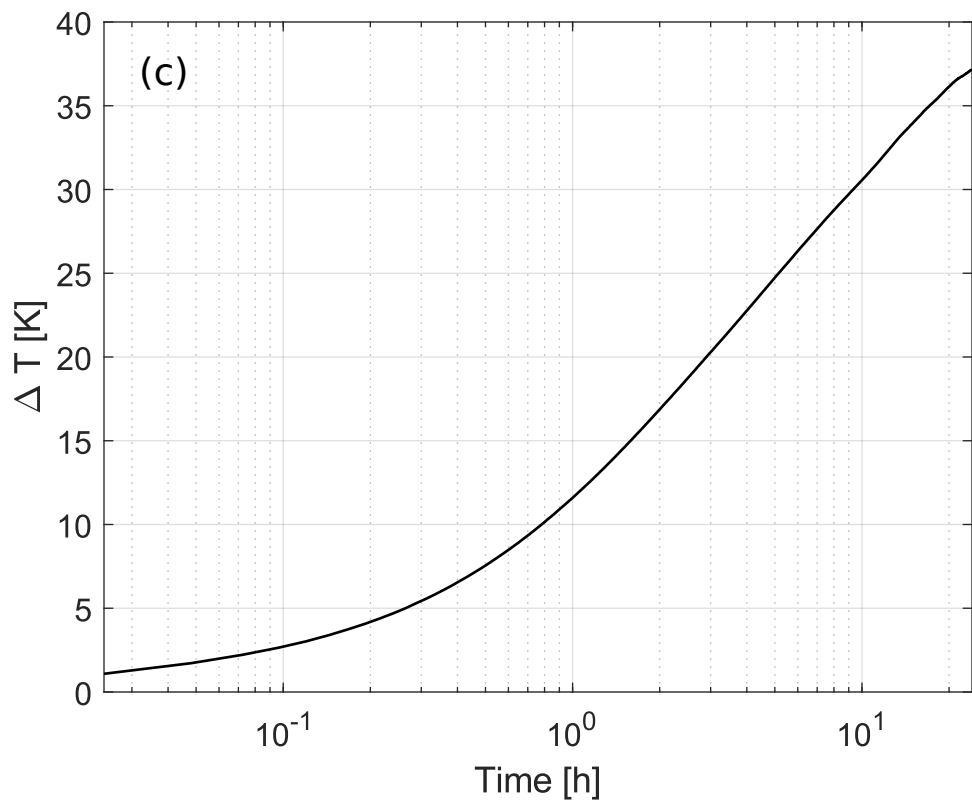
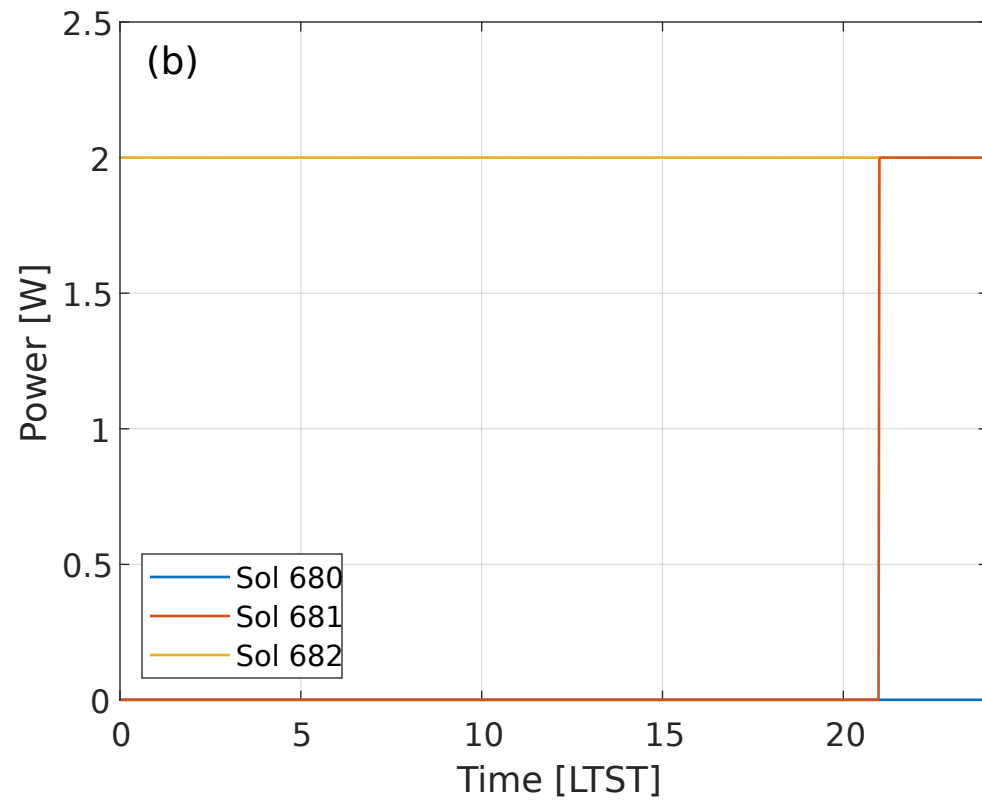
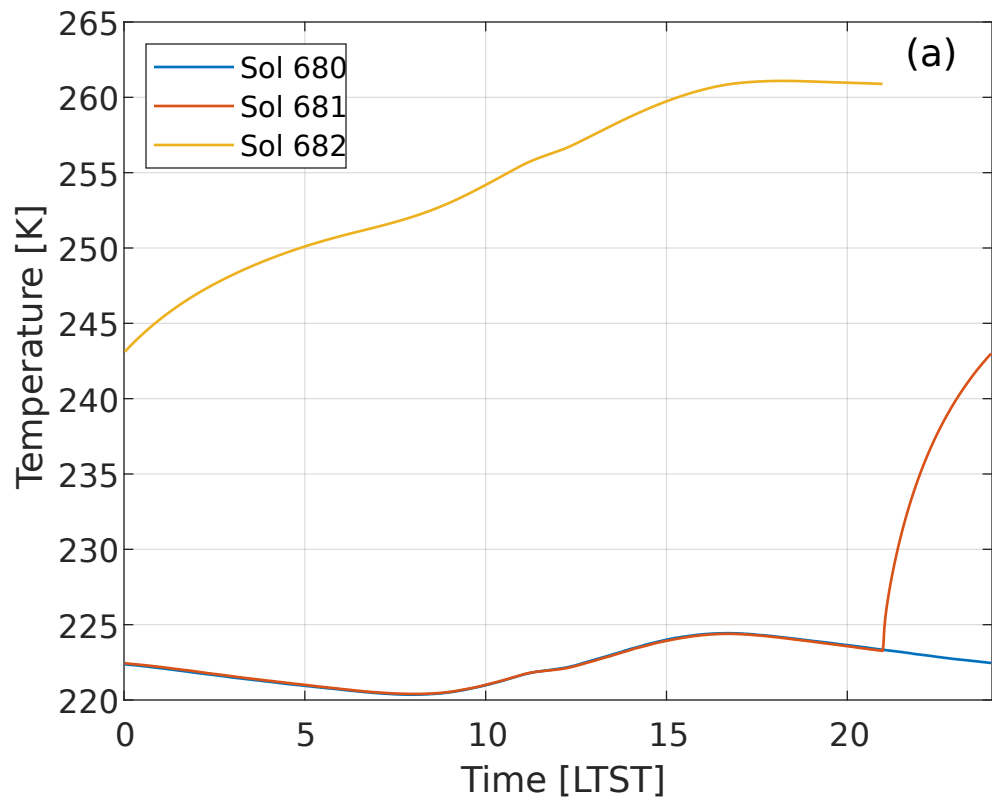


Figure 3.

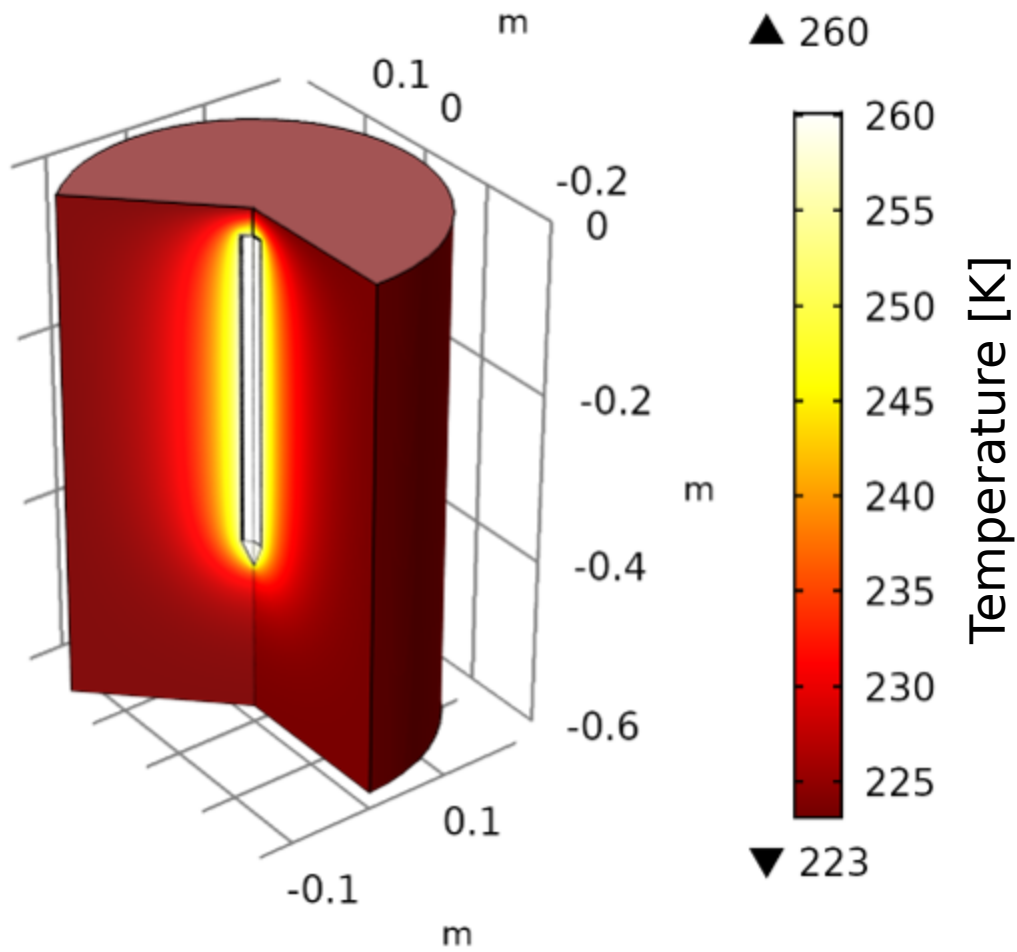


Figure 4.

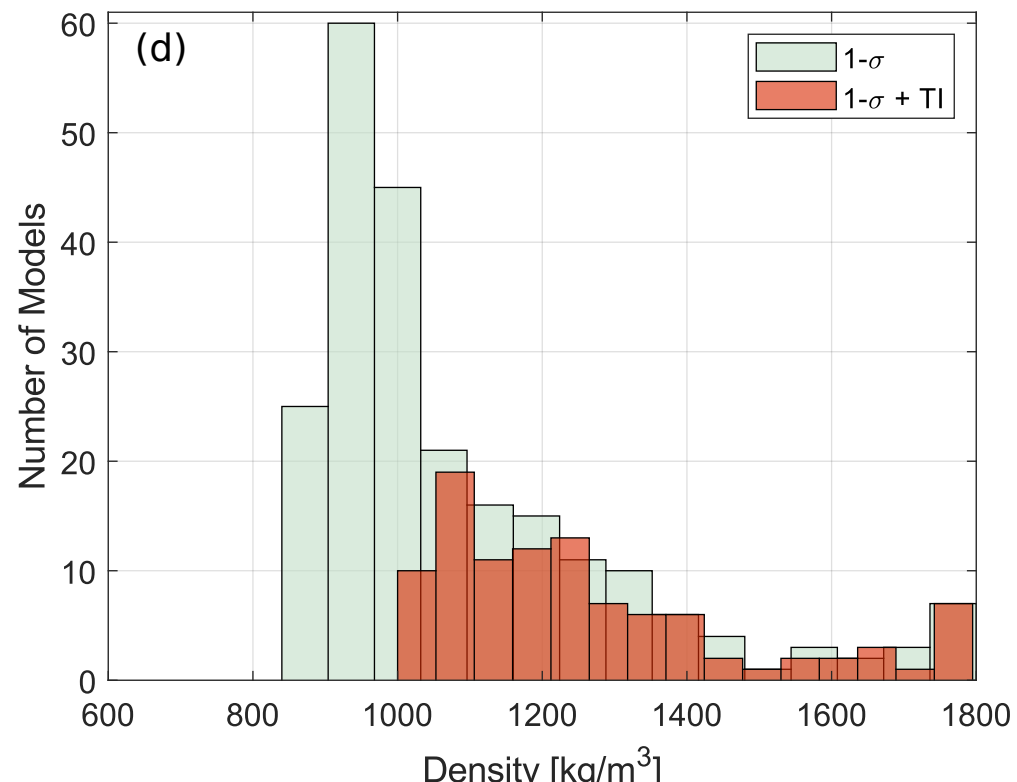
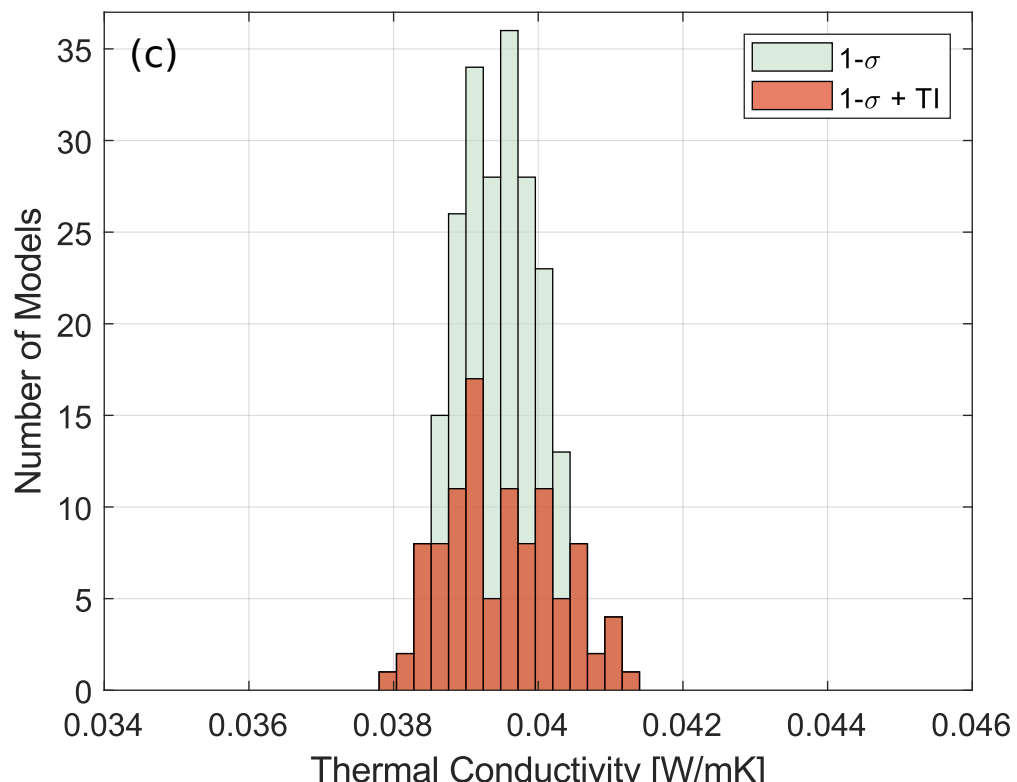
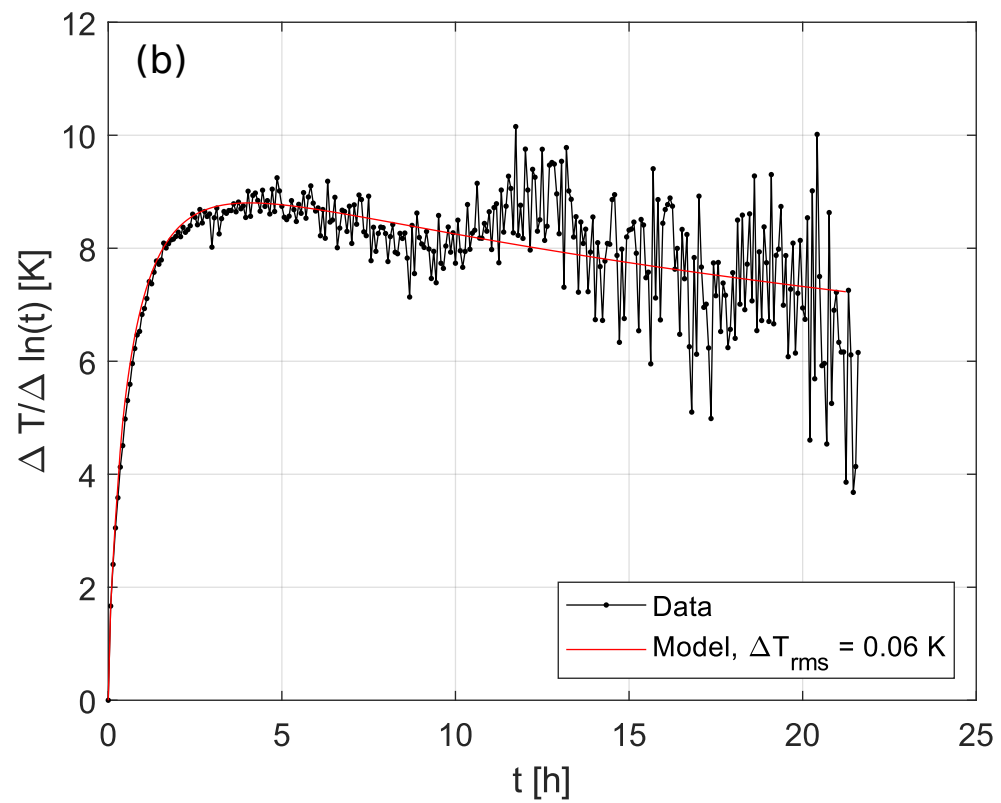
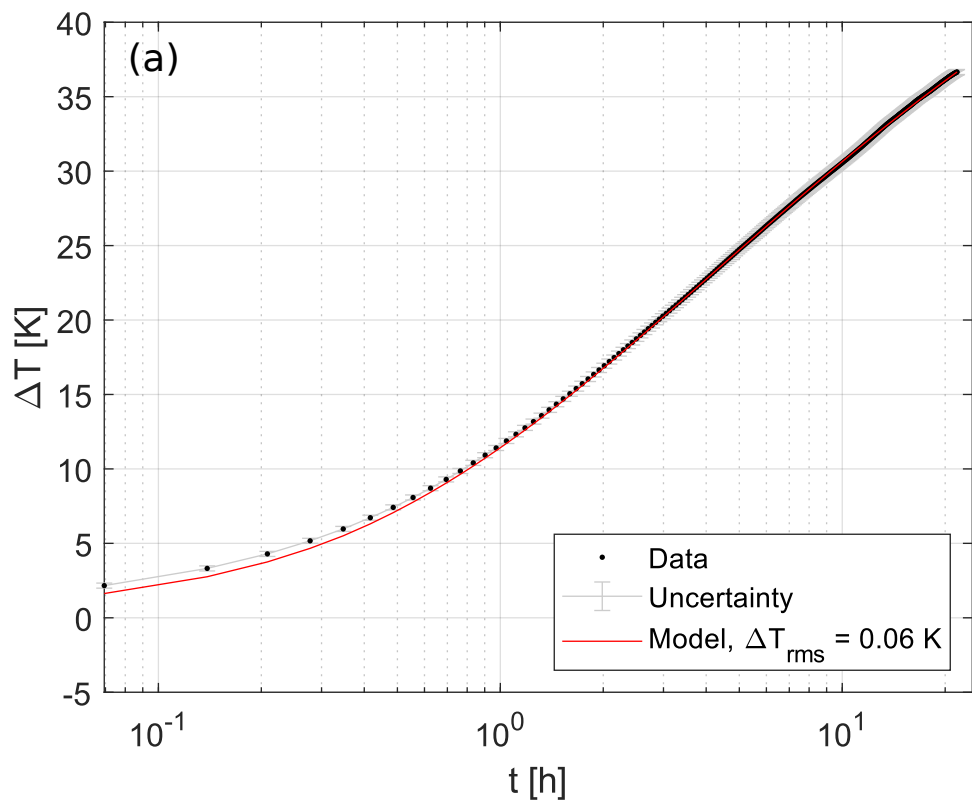


Figure 5.

